Structural stiffening in the human middle ear due to static pressure : finite-element analysis of combined static and dynamic middle-ear behavior

Structural stiffening in the human middle ear due to static pressure: Finite-element analysis of combined static and dynamic middle-ear behavior

Pieter G.G. Muyshondt[a,1], Joris J.J. Dirckx[a]

[a] *University of Antwerp, Biophysics and Biomedical Physics, Groenenborgerlaan 171, 2020 Antwerp, Belgium*

[1] Corresponding author; *E-mail:* pieter.muyshondt@uantwerpen.be

Abstract

The vibration response of the middle ear (ME) to sound changes when static pressure gradients are applied across the tympanic membrane (TM). To date, it has not been well understood which mechanisms lead to these changes in ME vibration response. In this study, a 3D finite-element model of the human ME was developed that simulates the sound-induced ME vibration response when positive and negative static pressures of up to 4 kPa are applied to the TM. Hyperelasticity of the soft-tissue components was considered to simulate large deformations under static pressure. Some ME components were treated as viscoelastic materials to capture the difference between their static and dynamic stiffness, which was needed to replicate both static and dynamic ME behavior. The change in dynamic stiffness with static preload was simulated by linearization of the hyperelastic constitutive model around the predeformed state. For the preloaded harmonic response, we found that the statically deformed ME geometry introduced asymmetry in the vibration loss between positive and negative pressure, which was due to the TM cone shape. As opposed to previous assumptions, the prestress in the ME due to static pressure had a substantial impact on the vibration response. We also found that material nonlinearity led to a higher stiffening at the umbo but a less pronounced stiffening at the footplate compared to the linear elastic condition. The results suggest that flexibility of the incudomalleolar joint (IMJ) enhances the decoupling of static umbo and footplate displacements, and that viscosity and viscoelasticity of the IMJ could play a role in the transfer of sound-induced vibrations from the umbo to the footplate. The components of the incudostapedial joint had minimal effect on ME mechanical behavior.

Keywords

middle-ear mechanics; finite-element model; hyperelasticity; viscoelasticity; pressure-induced hearing loss

---

Abbreviations: AML, anterior malleolar ligament; CT, computed tomography; FE, finite element; IMJ, incudomalleolar joint; ISJ, incudostapedial joint; LML, lateral malleolar ligament; ME, middle ear; PF, pars flaccida; PIL, posterior incudal ligament; PT, pars tensa; SAL, stapedial annular ligament; SML, superior malleolar ligament; SMT, stapedial muscle tendon; TA, tympanic annulus; TM, tympanic membrane; TMC, tympano-malleolar connection; TTT, tensor tympani tendon

1. Introduction

Hearing is affected by changes in the static pressure in the middle-ear (ME) air space relative to the atmospheric pressure. Several researchers have measured the effect of static pressure on hearing in animals and humans by cochlear microphonics (e.g., Wever and Lawrence, 1954; Rahm et al., 1956) and audiometry (e.g., von Békésy, 1932; Loch, 1942; Hansen, 1955; Huizing, 1960; Finkelstein et al., 1992; Rasmussen, 1946; Bezold, 1887). A loss of hearing ability was observed at both negative and positive pressure changes, especially at low frequencies. The hearing loss due to static pressure is linked to changes in sound conduction through the ME. In the clinic, static pressure loads have been used to investigate the vibroacoustic transfer of the ME by tympanometry. With this technique, the ME impedance or admittance is measured while the static pressure is varied in the ear canal (Shanks and Shelton, 1991). Although tympanometry can give meaningful insights into the vibroacoustic behavior of the ME, it only uses the overall acoustic signal reflected by the tympanic membrane (TM). However, it provides no information about the spatial variation of the ME response under static pressure. To collect spatial information of vibroacoustic changes in the ME, researchers have measured the ME vibration response under static pressure in animal and human temporal-bone experiments by different point measurement techniques. In animals, the changes in TM vibration due to positive and negative ME pressure were measured by holographic interferometry in canine (Suehiro, 1990) and laser Doppler vibrometry in gerbil (Lee and Rosowski, 2001; Rosowski and Lee, 2002). In human temporal bones, the changes in vibration response of the umbo and stapes footplate were measured by a non-contact optical vibration sensor (Gyo and Goode, 1987), a stroboscopic video measuring system (Murakami et al., 1997) and a laser Doppler vibrometer (Gan et al. 2006; Homma et al., 2010). It was shown that umbo and footplate vibrations are mainly reduced at low frequencies and that positive and negative pressures have different effects on the dynamic TM and stapes response, which may be governed by various mechanisms of structural stiffening.

To improve understanding of the mechanisms behind the changes in ME vibration response due to static pressure, researchers have developed finite-element (FE) models that simulate the sound-induced vibration response of the ME under simultaneous acoustic and static pressure loading (Wang et al., 2007; Homma et al., 2010; Ihrle et al., 2013; Zhang et al., 2020). These models succeeded at replicating many of the observed changes in ME vibration under static pressure. However, some of the static and dynamic mechanical properties of the ME components were determined on a phenomenological basis to obtain a good agreement with experimental data. Therefore, it remains unclear which underlying mechanisms contribute to the changes in ME dynamics under static pressure, and to what extent they have influence. According to Homma et al. (2010), the

dynamic properties of the ME are affected by changes in the ME geometry with the static pressure, the prestress in the ME components due to the static preload, and the material nonlinearity associated with the nonlinear elastic deformation of the soft-tissue structures.

In this work, we present a 3D FE model of the ME based on a micro-CT scan of a human temporal bone to investigate the sound-transfer function of the ME under positive and negative static pressure. To describe the static deformation of the ME due to static pressure, we considered material nonlinearity of the ME components in addition to geometric nonlinearity by treating the soft-tissue structures as hyperelastic materials. Several parts were modeled as viscoelastic materials to capture the variation of the dynamic stiffness and damping with the excitation frequency. We evaluated the quantitative effects of the deformed geometry, material nonlinearity and prestress due to static pressure on the ME vibration response. As it is believed that the ossicular joints of the ME play a role in the static and vibroacoustic behavior of the ME, we investigated the influence of the incudomalleolar joint (IMJ) and incudostapedial joint (ISJ) on the model results. We simulated the joints in detail by considering the capsule, synovial gap and cartilage layers in the joints. A sensitivity analysis was done to compare the influence of the elastic parameters in the model on the unloaded and preloaded vibration response.

2. Materials and methods

2.1 Geometry generation

The geometry of the FE model was based on a micro-CT scan of a fresh frozen human temporal bone (male, 73y) that was made at the Center for X-Ray Tomography of Ghent University (sample 3 in De Greef et al., 2015). The sample was stained using phosphotungstic acid (PTA) before scanning to improve soft-tissue contrast with minimal volume shrinkage (Buytaert et al., 2014). The reconstructed scan had a voxel pitch of 22.8 µm. After reconstruction, the scan was segmented using semi-automatic tools and manual operations in Amira 6.3 (FEI, Hillsboro, OR, USA). For more information about the sample preparation, scanning and image segmentation procedures, we refer the reader to De Greef et al. (2015). For the present work, we slightly adapted the segmented data set to divide the two ossicular joints into their structural components, identifying the capsule, cartilage layers and synovial gap, which was done by manual segmentation. The cartilage layers in the model entirely covered the interfaces between the synovial gap and the internal surfaces of the ossicles. Next, the segmented data set was converted into a triangulated surface model as described in De Greef et al. (2017). The final surface model consisted of approximately 25,000 triangles. Fig. 1 shows the triangulated surface model

indicating all components included in the FE model. Some ligaments observed in the micro-CT scan were not incorporated in this model because they are not present in all individuals (De Greef et al., 2015), that is, for ligaments with an occurrence of 83% or less. Figs. 2 and 3 show the internal structure of the IMJ and ISJ, respectively. As can be seen in Fig. 3, the ISJ capsule ranged from the rim of the stapes head to the proximal end of the incus lenticular process, hence completely embedding the lenticular process. This configuration is in agreement with the findings of Karmody et al. (2009) in their the anatomical study of the ISJ.

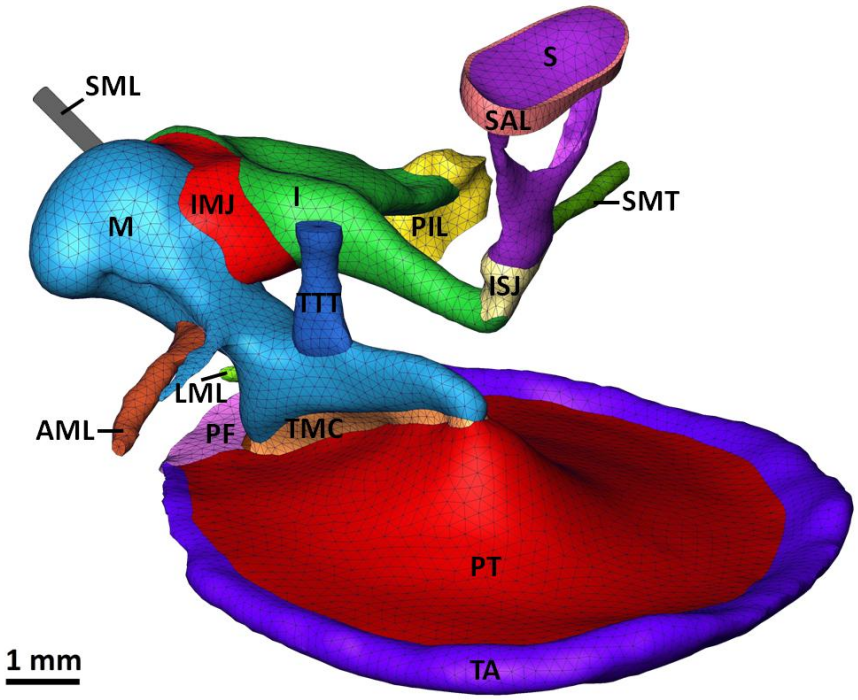

Fig. 1. Triangulated surface model of the ME (anteroinferior view). The different components included in the model are indicated: AML, anterior malleolar ligament; I, incus; IMJ, incudomalleolar joint; ISJ, incudostapedial joint; LML, lateral malleolar ligament; M, malleus; PF, pars flaccida; PIL, posterior incudal ligament; PT, pars tensa; S, stapes; SAL, stapedial annular ligament; SML, superior malleolar ligament; SMT, stapedial muscle tendon; TA, tympanic annulus; TMC, tympano-malleolar connection; TTT, tensor tympani tendon.

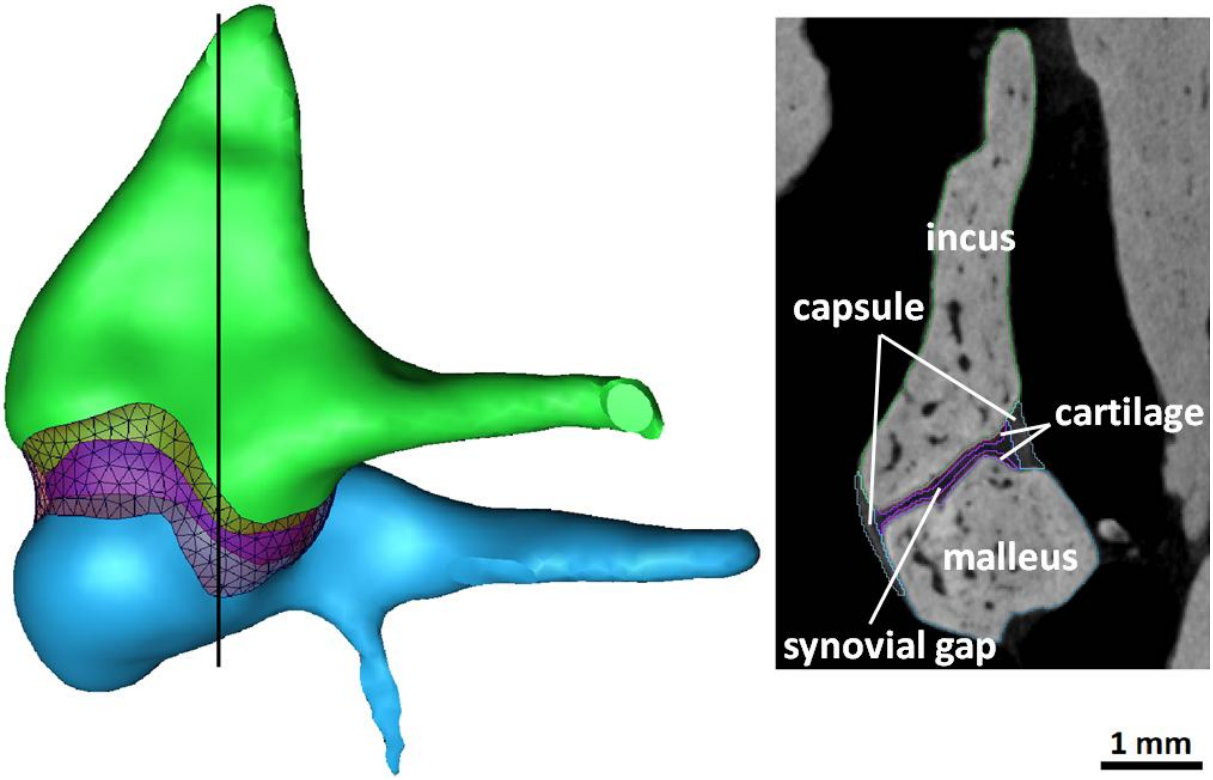

Fig. 2. Medial view of the incudomalleolar (IM) complex depicted by a 3D surface model (left) and a tomographic cross-section showing the components inside the joint (right). The vertical line in the surface model annotates the location of the cross-section through the IM complex. The triangulated mesh in the 3D model depicts the joint capsule, which is made partially transparent to expose the underlying synovial gap.

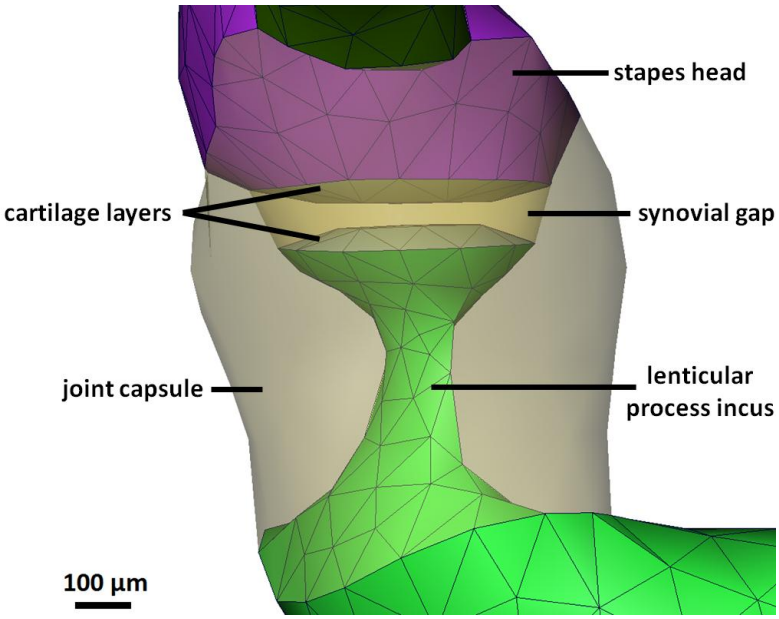

Fig. 3. Posterior view of the ISJ with internal components indicated. The joint capsule and synovial gap are made partially transparent to visualize the underlying structures, including the lenticular process of incus, head of stapes and cartilage layers.

2.2 Geometric model properties

The FE simulations were performed in the commercial FE software COMSOL Multiphysics 5.5 (COMSOL Inc, Burlington, MA, USA), extended with the Structural Mechanics Module and the Nonlinear Structural Materials Module. The imported triangular surface model of the ME was converted to a volumetric mesh composed of tetrahedral elements. As in our previous FE model (De Greef et al., 2017) we modeled all components as second-order (quadratic) solid elements, including for the pars tensa (PT) and pars flaccida (PF) of the TM. It has been shown that the thickness of the TM has a substantial effect on the static and dynamic ME response (e.g., Volandri et al., 2011; Rohani et al., 2017). Because TM thickness cannot be determined accurately with micro-CT, we used the average TM thickness distribution measured with optical coherence tomography by Van der Jeught et al. (2013). As the geometry of the TM in the current model differs from the geometry of the average TM in Van der Jeught et al. (2013), the average TM thickness map in Van der Jeught et al. (2013) was remapped onto the current TM geometry. This was achieved by rescaling the circumferential contour of the average TM so it matched with the circumferential contour of the current TM. The contour was rescaled in the radial direction around the umbo inside the plane formed by the TM circumference, as described in Van der Jeught et al. (2013). The average thickness values over the TM surface were remapped to the current TM accordingly. To create a solid of the TM with appropriate thickness distribution, the vertices on the lateral surface of the TM geometry were displaced in the medial-to-lateral direction such that the distance to the medial surface of the TM was equal to the desired thickness at each point. Because the distance was defined and set in the medial-to-lateral direction, we made use of the average thickness distribution obtained with Z-projection (Van der Jeught et al., 2013), which is based on the same definition. The average TM thickness distribution obtained with Z-projection, remapped onto the current TM model, is shown in Fig. 4. A single layer of elements was considered through the thickness of the TM, because changing the number of layers to two had minimal effect on the static stresses in the TM and the umbo and footplate vibration responses (< 0.1 dB).

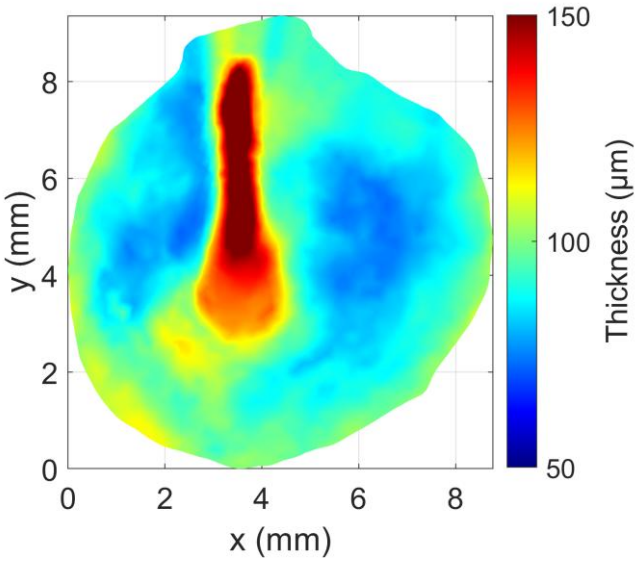

Fig. 4. Thickness distribution of the TM (PT and PF) used in the FE model. The thickness map corresponds to the average thickness measured by Van der Jeught et al. (2013) using optical coherence tomography, and was remapped onto the TM of the current model. We used the Z-projection technique of Van der Jeught et al. (2013) to establish the thickness of the geometric TM model.

2.3 Boundary conditions and loads

For all simulations, the distal ends of the ligaments and tendons and the outer perimeters of the TA and SAL were constrained by setting the three translational degrees of freedom at the corresponding faces to zero. The locations of these constraints are given by the anterior wall of the tympanic cavity for the AML, the posterior aspect of the tympanic notch for the LML, the roof of the tympanic cavity for the SML, the incudal fossa for the PIL, and the posterior wall of the tympanic cavity for the SMT. Distally, the TTT in the model ends at the point where it makes a sharp bend around the processus cochleariformis at the tympanic cavity wall. The constrained perimeter of the TA is attached to the tympanic sulcus and the perimeter of the SAL to the oval window. The PF is constrained superiorly at its attachment to the petrous bone at the notch of Rivinus.

The load of the cochlea was modeled by a uniform pressure $p_C = Z_C v_{FP} A_{FP}$ on the medial surface of the stapes footplate. In this equation, Z_C is the acoustic impedance of the cochlea, which was obtained by averaging measurements of the human cochlear acoustic impedance available in the literature (Merchant et al. 1996; Puria et al., 1997; Aibara et al. 2001; Nakajima et al. 2009). In this calculation, we took a weighted average where the contribution of each study was proportional to the number of measured TBs (n) in that study (n = 1 for Merchant et al., 1996; n = 4 for Puria et al., 1997; n = 12 for Aibara et al., 2001; n = 6 for Nakajima et al., 2009). The magnitude and phase of Z_C obtained in this way are shown in Fig. 5. The variable v_{FP} represents the out-of-plane

velocity at the footplate center. By evaluating the footplate velocity at the center point, there was only a contribution of piston-like footplate motion to v_{FP} and hence p_{C}. The minor contribution of footplate rocking motion to the cochlear load that has been experimentally observed (Dobrev et al., 2018) was disregarded. The surface area of the footplate A_{FP} = 3.2 mm^2 corresponds to the value that was used to determine Z_{C} experimentally. The cochlear load in the model only had a contribution to the dynamic simulations and not the static simulations. This assumption is in agreement with experiments on gerbil ears, in which removing the cochlear fluid had no considerable effect on the ME deformation due to static pressure (Dirckx and Decraemer, 2001).

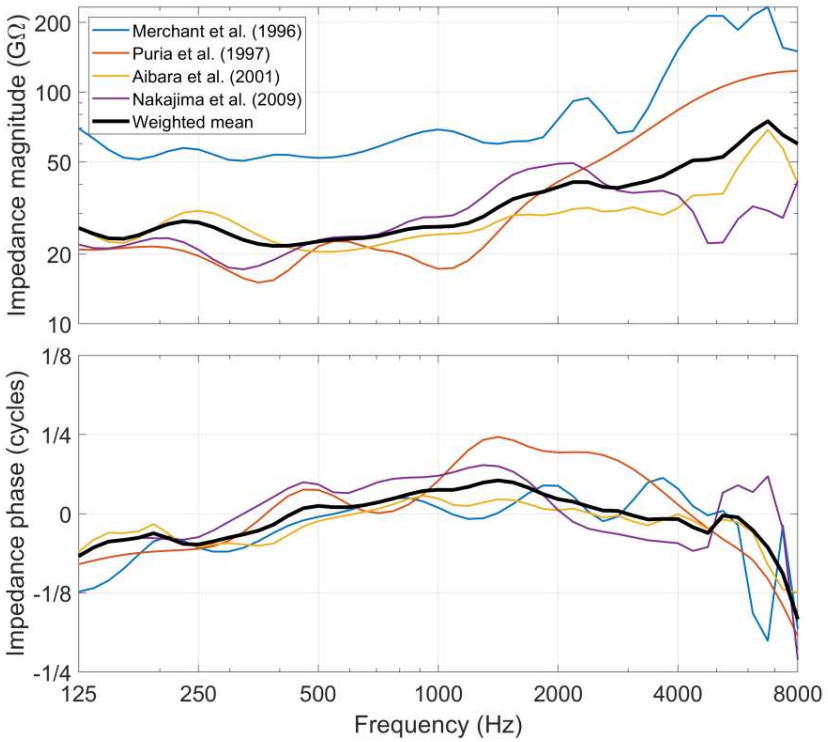

Fig. 5. Magnitude and phase of the acoustic input impedance of the cochlea (1 GΩ = 10^9 Pa s/m^3) obtained from the mean data of four experimental studies. To calculate overall mean of the experiments, the weight of each experimental curve was taken proportional to the number of measured samples in the corresponding study.

The excitation loads in the model were represented by a uniform pressure on the lateral surface of the TM, i.e., the PT and PF. For the static simulations, the static pressure ranged from 0 kPa to either –4 or +4 kPa, which corresponds to the maximal range used in clinical tympanometry. In the present work, static pressures will be called positive (resp. negative) when the pressure in the ear canal is higher (resp. lower) than in the ME cavity. For the (linear) harmonic frequency-domain simulations, we applied a harmonic pressure of 1 Pa amplitude to the TM surface such that the linear vibration response of the ME was normalized to input pressure. The

assumption of uniformity of the sound-pressure field is consistent with observations of Bergevin and Olson (2014) in gerbil. The ear canal was not included in the model because the simulations are compared to experiments in which the sound pressure was measured close to the TM surface (Murakami et al., 1997; Gan et al., 2006; Homma et al., 2010).

In both the static and dynamic simulations, we ignored the acoustic impedance of the ME cavity, which may consist of a compliance, radiance and inertance component. The acoustic compliance of the cavity may affect both static and dynamic behavior, and was incorporated in, e.g., Motallebzadeh et al. (2017). However, we compared our model to temporal-bone experiments in which the static pressure or sound pressure was applied and measured on either the ear-canal side or ME-cavity side, while the air space on the opposite side of the TM was not explicitly sealed airtight (Murakami et al., 1997; Gan et al., 2006; Homma et al., 2010). Therefore, the effect of cavity compliance was canceled. The acoustic radiance of the ME cavity (real part of the impedance) may contribute to the dynamic behavior. Yet, Maftoon et al. (2015) estimated that it has little effect compared to the ME and cochlear impedance, so we neglected it. The acoustic inertance or mass load of the ME cavity, which might affect the dynamic behavior, was ignored as in Maftoon et al. (2015) and Motallebzadeh et al. (2017).

2.4 Elastic material properties

For the static simulations, large static pressures of up to 4 kPa were applied to the lateral TM surface, which cause large deformations. Therefore, geometric nonlinearity was incorporated in the static simulations, taking into account the effect of the change in geometric configuration on ME deformation with accumulating static pressure. In addition to geometric nonlinearity, we took into account hyperelasticity of the ME soft-tissue structures to describe the nonlinear elastic deformation of the ME. We made use of the Veronda–Westmann model (Veronda and Westmann, 1970), as it is suited to describe the nonlinear stress-strain relationship of soft biological tissues up to relatively high degrees of strain, while using only two material parameters. Hyperelastic models for nonlinear elastic isotropic materials are described by a strain-energy function W, which is often split into an isochoric part W_{iso} and a volumetric part W_{vol} as follows:

$$W = W_{\mathrm{iso}}(\bar{I}_1, \bar{I}_2) + W_{\mathrm{vol}}(J). \tag{1}$$

In this equation, $J = \sqrt{\det(\mathbf{C})} = \lambda_1\lambda_2\lambda_3$, where λ_i are the three principal stretches of the material ($i = 1,2,3$) and $\mathbf{C}$ is the right Cauchy–Green deformation tensor defined by $\mathbf{C} = \mathbf{F}^{\mathrm{T}}\mathbf{F}$. The tensor $\mathbf{F} = \partial\mathbf{x}/\partial\mathbf{X}$ is the deformation gradient, with $\mathbf{x}$ and $\mathbf{X}$ the position vectors of the solid in the deformed and undeformed configuration, respectively. In Eq. (1), $\bar{I}_1 = J^{-2/3}I_1$ and $\bar{I}_2 = J^{-4/3}I_2$, with $I_1 = \mathrm{tr}(\mathbf{C}) = \lambda_1^2 + \lambda_2^2 + \lambda_3^2$ the first

invariant and $I_2 = [\mathrm{tr}(\mathbf{C})^2 - \mathrm{tr}(\mathbf{C}^2)]/2 = \lambda_1^2\lambda_2^2 + \lambda_2^2\lambda_3^2 + \lambda_3^2\lambda_1^2$ the second invariant of $\mathbf{C}$. W_{iso} describes the isochoric (or deviatoric) deformation behavior of the material, and is defined for the Veronda–Westmann model as

$$W_{\mathrm{iso}} = \mu\left[\frac{\mathrm{e}^{b(\bar{I}_1-3)} - 1}{b} - \frac{\bar{I}_2 - 3}{2}\right]. \tag{2}$$

In this equation, μ is the shear modulus of the material in the limit of zero strain (or $\lambda_i = 1$) and b is a parameter that describes the change of stress with the strain. For the volumetric behavior, we assumed that the hyperelastic components are incompressible, which is a reasonable assumption for soft biological tissue. In that case, W_{vol} is replaced by the expression $-p(J-1)$, where p is a hydrostatic pressure that functions as a Lagrange multiplier to enforce the incompressibility constraint $J = 1$. For a more extensive description of the theory of finite deformation elasticity, we refer the reader to Başar and Weichert (2000) and Merodio and Ogden (2020).

The hyperelastic behavior of the ME components was measured by uniaxial tensile tests on the PT (Cheng et al., 2007), stapedial muscle tendon (SMT) (Cheng and Gan, 2007), tensor tympani tendon (TTT) (Cheng and Gan, 2008a), and anterior malleolar ligament (AML) (Cheng and Gan, 2008b). Zhang and Gan (2011) performed uniaxial tension and compression test on the ISJ capsule, and Gan et al. (2011) did simple shear tests on the stapedial annular ligament (SAL). In these studies, an incompressible hyperelastic first-order Ogden model was used to describe the nonlinear elastic deformation behavior, which is defined by the isochoric strain-energy function

$$W_{\mathrm{iso}} = \frac{2\mu_1}{\alpha_1^2}\left(\lambda_1^{\alpha_1} + \lambda_2^{\alpha_1} + \lambda_3^{\alpha_1} - 3\right), \tag{3}$$

with μ_1 the shear modulus in the limit of zero strain, α_1 a parameter that determines the change of stress with the strain, and $\lambda_1\lambda_2\lambda_3 = 1$. For this type of material, the engineering stress T under uniaxial tension and the shear stress τ under simple shear are defined by

$$T = \frac{2\mu_1}{\alpha_1}\left(\lambda^{\alpha_1-1} + \lambda^{-\alpha_1/2-1}\right). \tag{4}$$

$$\tau = \frac{\mu_1}{\alpha_1}\frac{1}{\sqrt{1+\gamma^2/4}}\left[\left(\frac{\gamma}{2} + \sqrt{1+\gamma^2/4}\right)^{\alpha_1} - \left(-\frac{\gamma}{2} + \sqrt{1+\gamma^2/4}\right)^{\alpha_1}\right], \tag{5}$$

with λ the stretch in the tensile direction and γ the shear strain (Mao, 2018). For the incompressible Veronda–Westmann model, T and τ are given by

$$T = 2\mu(\lambda - \lambda^{-2})\left[\mathrm{e}^{b\left(\lambda^2+2\lambda^{-1}-3\right)} - \frac{1}{2\lambda}\right], \tag{6}$$

$$\tau = 2\mu\gamma\left(\mathrm{e}^{b\gamma^2} - \frac{1}{2}\right). \tag{7}$$

To determine the values of μ and b for the PT, SMT, TTT, AML and SAL we fitted the stress-strain relations of the Veronda-Westmann model in Eqs. (6)–(7) to the stress–strain relationships of the Ogden model in Eqs. (4)–(5). In Eqs. (4)–(5), μ_1 and α_1 were taken from the studies that fitted the Ogden model to experimentally obtained stress–strain curves (Motallebzadeh, et al. 2013; Cheng and Gan, 2007, 2008a–b; Gan et al., 2011). For the ISJ capsule, we used the Veronda–Westmann parameters determined by Soleimani et al. (2020). We calculated the values of μ and b by minimizing the sum of squared differences between Eqs. (4) and (6) for uniaxial tension, and between Eqs. (5) and (7) for simple shear, using the *fminsearch* function in MATLAB. The strain range over which we performed the minimization was determined by the maximal tensile strain $\varepsilon = \lambda - 1$ and shear strain γ used in the experiments, which was equal to ε = 0.15 for the PT (Cheng et al., 2007), ε = 0.4 for the SMT, TTT and AML (Cheng and Gan, 2007, 2008a, 2008b), and γ = 3 for the SAL (Gan et al., 2011). The hyperelastic parameters determined in this way were used in the FE model. One exception was the shear modulus of the PT μ_{PT}, for which we chose a value that gave a good match with static and dynamic experimental data. The motivation for this approach was that the Young's modulus of the TM in human E_{PT} (= $3\mu_{\mathrm{PT}}$ in the case of incompressibility) has been determined in multiple studies, showing great diversity in the results with values ranging from 0.4 to 300 MPa (see for example the summary of Rohani et al., 2017). In our model, the value μ_{PT} = 10 MPa (E_{PT} = 30 MPa) was found to be appropriate. It has been suggested that the elasticity of the TM is orthotropic, with different Young's moduli in the radial and circumferential direction due to the specific organization of the collagen fiber layers in the membrane. O'Connor et al. (2017) investigated how the layered and orthotropic fibrous structure of the TM affects the ME response by considering the Young's moduli of the TM in the three orthotropic directions (radial, circumferential and transversal). These Young's moduli were decoupled from the TM shear modulus in their study, assuming that relative sliding of the fibers is possible. They found that an appropriate combination for the values of the orthotropic TM Young's moduli, TM shear modulus and TA Young's modulus produced a ME response comparable to measurements, which could also be approximated when using a fully isotropic TM Young's modulus of 20 MPa. Because the difference between the radial and circumferential TM Young's modulus has not been very clear in experiments (Luo et al., 2009) and for the sake of simplicity, we used an isotropic elastic description for the TM as for all other components.

For the ME components of which no hyperelastic data was available, we used hyperelastic parameters from other ME tissues, elastic parameters used in previous models, or parameter values that resulted in a good match with experimental data. For the lateral malleolar ligament (LML), superior malleolar ligament (SML) and posterior incudal ligament (PIL), we used the same hyperelastic parameters as for the AML. For the PF, TA and TMC we used the same value of b as for the PT, but for μ we used a smaller value than that of the PT. For the TMC it has been found that a Young's modulus of 10% of the PT Young's modulus results in a good agreement with vibration data on the lateral and medial side of the manubrium (De Greef et al., 2014). For the PF, which is a continuation of the ear-canal skin (Lim, 1968), it is generally accepted that the Young's modulus is lower than for the PT. For the TA, the Young's moduli that have been used in FE models were typically lower than for the PT (e.g., Gan et al., 2004; Homma et al., 2010). In the current model, we used a value of μ = 1 MPa for the PF, TA and TMC, which is ten times lower than μ_{PT}. The synovial gap of the ISJ was modeled as a very flexible incompressible linear elastic material to mimic its fluid behavior; incompressibility was enforced by the expression $-p(J-1)$ with the constraint $J = 1$, and the very soft elastic shear behavior was simulated by using the shear part of the Saint-Venant Kirchhoff strain-energy function $\mu\mathbf{E}\colon\mathbf{E}$. In this expression, $\mathbf{E} = 1/2\,(\mathbf{C}-\mathbf{I})$ is the Green–Lagrange strain tensor, with $\mathbf{I}$ the identity matrix and μ the shear modulus. This type of material is an extension of the infinitesimal theory of linear elasticity to the nonlinear deformation regime (Başar and Weichert, 2000). Therefore, a linear relationship is assumed between the second Piola-Kirchhoff stress $\mathbf{S}$ and Green–Lagrange strain $\mathbf{E}$, which describe the stress and strain in the undeformed configuration of the solid, respectively. We chose a value for μ that was small enough to obtain a good match with static deformation data of the ME, but not too small to ensure convergence of the nonlinear solver for static pressures up to +4 and –4 kPa. These conditions were met for a value of μ = 1 kPa. The cartilage layers in the ISJ were modeled as linear elastic materials with a Young's modulus of E = 10 MPa and a Poisson's ratio of ν = 0.3, which is the same as in Zhang and Gan (2011) and Soleimani et al. (2020). For the IMJ components we used the same elastic parameters as for the ISJ components. The only exception was the parameter b of the IMJ capsule, for which we used the value of 22.02 from the PT instead of 1.8 as it gave a better agreement with static deformation data under negative ear-canal pressure. The bony ossicles were modeled as linear elastic materials with a Young's modulus of E = 16 GPa, which is equal to the average value measured by Soons et al. (2010) on the malleus and incus in rabbit. For the Poisson's ratio of the ossicles we used a value of ν = 0.3. The elastic parameters of all components are summarized in Table 1. Fig. 6 (left) shows the engineering stress T as a function of engineering strain ε for

all hyperelastic materials investigated by uniaxial tension. Fig. 6 (right) depicts the shear stress τ as a function of shear strain γ for the SAL, which was measured by simple shear tests.

Table 1. Elastic parameters of the ME components used in the base model. For the PT, SMT, TTT, AML and SAL, we calculated μ and b by fitting the Veronda–Westmann model to the corresponding first-order Ogden model defined by μ_1 and α_1 in the given sources. [a] Optimized by manual adjustment to obtain realistic static and dynamic ME behavior. [b] Typically lower than μ_{PT}; optimized by manual adjustment. [c] The same value as b_{PT} was used to obtain more realistic static behavior at negative pressure. [d] Small enough to match static deformation data, but large enough to ensure convergence of the nonlinear solver.

Incompressible hyperelastic Veronda–Westmann materials			
Component	μ (MPa)	b	*Source*
PT	10[a]	22.02	Motallebzadeh et al. (2013): μ_1 = 0.4 MPa, α_1 = 28.8
PF	1[b]	22.02	PT
TMC	1[b]	22.02	PT
TA	1[b]	22.02	PT
SMT	0.084	5.97	Cheng and Gan (2007): μ_1 = 0.05 MPa, α_1 = 17.4
TTT	0.031	8.88	Cheng and Gan (2008a): μ_1 = 0.01 MPa, α_1 = 23.52
AML	0.102	4.11	Cheng and Gan (2008b): μ_1 = 0.078 MPa, α_1 = 13.69
LML	0.102	4.11	AML
SML	0.102	4.11	AML
PIL	0.102	4.11	AML
SAL	$9.72 \cdot 10^{-3}$	0.214	Gan et al. (2011): μ_1 = 3.28 kPa, α_1 = 5.9
ISJ capsule	0.126	1.8	Soleimani et al. (2020)
IMJ capsule	0.126	22.02[c]	ISJ capsule
Linear elastic materials			
Component	E (MPa)	ν	*Source*
malleus, incus and stapes	$16 \cdot 10^3$	0.3	Soons et al. (2010)
ISJ cartilage	10	0.3	Soleimani et al. (2020)
IMJ cartilage	10	0.3	ISJ cartilage
Incompressible linear elastic materials			
Component	μ (MPa)		*Source*
ISJ synovial gap	$1 \cdot 10^{-3}$ [d]		/
IMJ synovial gap	$1 \cdot 10^{-3}$ [d]		/

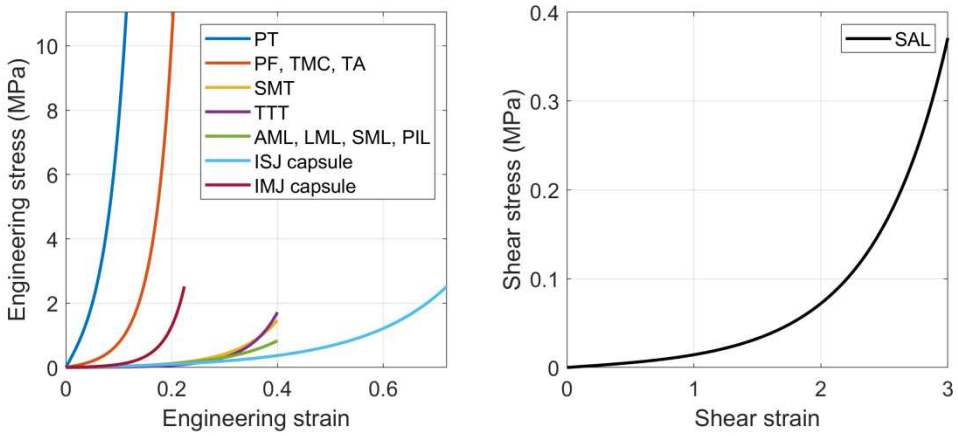

Fig. 6. Stress-strain curves of the hyperelastic components in the model. Engineering stress as a function of engineering strain for uniaxial tension (left). Shear stress as a function of shear strain for simple shear deformation (right).

2.5 Viscoelastic, damping and mass properties

For dynamic simulations, both elastic and viscous effects contribute to the mechanical response of a solid. In this model, the dynamic behavior is represented by small harmonic oscillations induced by sound-pressure excitation. It is often assumed that viscoelasticity is associated with shear deformation as opposed to volumetric deformation. In that case, the time-dependent relation between the shear stress and shear strain in the solid is described by a shear relaxation function $G(t)$, which is often represented by a Prony series associated with the generalized Maxwell model:

$$G(t) = G_\infty + \sum_{i=1}^{n} G_i \mathrm{e}^{-t/\tau_i}. \tag{8}$$

In Eq. (8), G_∞ is the long-term shear modulus of the elastic branch in the generalized Maxwell model that describes the shear behavior as $t \to \infty$ when all transient stresses and strains have been relaxed, n is the number of viscoelastic branches in the model, G_i is the shear modulus of the ith branch, and τ_i is the corresponding relaxation time. The shear modulus for $t \to 0$ is denoted the instantaneous shear modulus $G_0 = G_\infty + \sum_{i=1}^{n} G_i$. Let us now introduce the nondimensional shear relaxation function $g(t) = G(t)/G_\infty - 1$, or

$$g(t) = \sum_{i=1}^{n} g_i \mathrm{e}^{-t/\tau_i}, \tag{9}$$

with $g_i = G_i/G_\infty$. $G(t)$ can be expressed in the frequency domain by taking the Fourier transform of the Prony series in Eq. (8). This operation leads to the definition of the complex shear modulus $G^*(\omega) = G_\infty[1 + i\omega g^*(\omega)]$, with ω the angular frequency, i the imaginary unit and $g^*(\omega)$ the Fourier transform of $g(t)$ given by

$$g^*(\omega) = \sum_{i=1}^{n} \frac{\tau_i g_i}{1 + i\omega\tau_i}. \tag{10}$$

$G^*(\omega)$ can be split into a real and imaginary part as $G^*(\omega) = G'(\omega) + iG''(\omega) = G'(\omega)[1 + i\eta(\omega)]$. $G'(\omega)$ is the storage modulus, $G''(\omega)$ the loss modulus, and $\eta(\omega) = G''(\omega)/G'(\omega)$ the loss factor, with

$$G'(\omega) = G_\infty \left(1 + \sum_{i=1}^{n} \frac{\omega^2 \tau_i^2 g_i}{1 + \omega^2 \tau_i^2}\right), \tag{11}$$

$$G''(\omega) = G_\infty \sum_{i=1}^{n} \frac{\omega \tau_i g_i}{1 + \omega^2 \tau_i^2}. \tag{12}$$

The viscoelastic properties of the ME have been studied for the PT, SAL and ISJ capsule at both long and short time scales. For long time scales in the range of 1–100 s (= low angular frequencies of 0.01–1 Hz), the viscoelastic behavior was studied most recently by Motallebzadeh et al. (2013) for the PT, Gan et al. (2011) for the SAL, and Soleimani et al. (2020) for the ISJ capsule. These studies were based on tensile or shear relaxation tests on the respective structures (Cheng et al., 2007; Gan et al., 2011; Zhang and Gan, 2011). From these studies, we derived a set of long time-scale parameters $g_i^L = G_i^L/G_\infty^L$ and τ_i^L describing the long time-scale or low-frequency viscoelastic shear behavior of the components. For short time scales in the range of 10^{-4}–10^{-2} s (= high angular frequencies of 10^2–10^4 Hz), the viscoelastic behavior was examined most recently by frequency-temperature superposition measurements in Zhang and Gan (2013a) for the PT, Zhang and Gan (2014) for the SAL, and Jiang and Gan (2018) for the ISJ capsule, which were based on tensile or shear tests. From these studies, we extracted a set of short time-scale parameters $g_i^S = G_i^S/G_\infty^S$ and τ_i^S describing the short time-scale or high-frequency viscoelastic shear behavior of the structures.

In the current model, we constructed viscoelastic models for the PT, SAL and ISJ capsule based on both the long and short time-scale parameters. In the harmonic simulations, we computed the vibration behavior in the frequency range of 0.125–8 kHz, which is covered mainly by the range of the short time-scale or high-frequency viscoelastic branches. However, the viscoelastic branches at long time scales or low frequencies can influence the magnitude of the storage modulus G' at high frequencies, affecting the high-frequency vibration behavior. To create a global viscoelastic model composed of long and short time-scale branches, we introduced the relaxation coefficients g_i with corresponding relaxation times τ_i. For the long time-scale branches in the global viscoelastic model, we used $g_i = g_i^L$ and $\tau_i = \tau_i^L$. For the short time-scale branches, we defined $g_i = g_i^S g_0^L$ and $\tau_i = \tau_i^S$, with $g_0^L = 1 + \sum_{i=1}^{n} g_i^L$ and n the number of long time-scale branches. The viscoelastic parameters of the global generalized Maxwell model determined in this way are given in Table 2. The corresponding storage moduli G'

and loss factors η were calculated using Eqs. (11)–(12) and are depicted in Fig. 7. The long-term shear moduli G_∞ that we used to create these graphs are given by the values of μ in Table 1, which represent the shear moduli in the absence of static predeformation. The frequency range investigated for the harmonic simulations is indicated in the graphs. From Fig. 7 (top), it becomes clear that G' is higher in the investigated frequency range than in the limit of zero frequency, where G' is given by G_∞. The viscoelastic parameters determined for the ISJ capsule were also used for the IMJ capsule in the model.

Table 2. Viscoelastic relaxation coefficients g_i and relaxation times τ_i used in the FE model obtained for the PT, SAL and ISJ capsule. The parameters determined for the ISJ capsule were also used for the IMJ capsule.

Component	g_i	τ_i (s)	*Source*
PT	0.1746	100	Motallebzadeh et al. (2013)
	0.1111	10	
	0.3016	1	
	0.6622	$5.72 \cdot 10^{-3}$	Zhang and Gan (2013a)
	0.8726	$85.1 \cdot 10^{-6}$	
SAL	0.3850	5.102	Gan et al. (2011)
	0.6924	$9.2 \cdot 10^{-3}$	Zhang and Gan (2014)
	0.7406	$117 \cdot 10^{-6}$	
ISJ and IMJ capsule	0.1	100	Soleimani et al. (2020)
	0.9	5	
	0.8619	$2.6 \cdot 10^{-3}$	Jiang and Gan (2018)
	1.3099	$140 \cdot 10^{-6}$	
	0.0825	$130 \cdot 10^{-6}$	

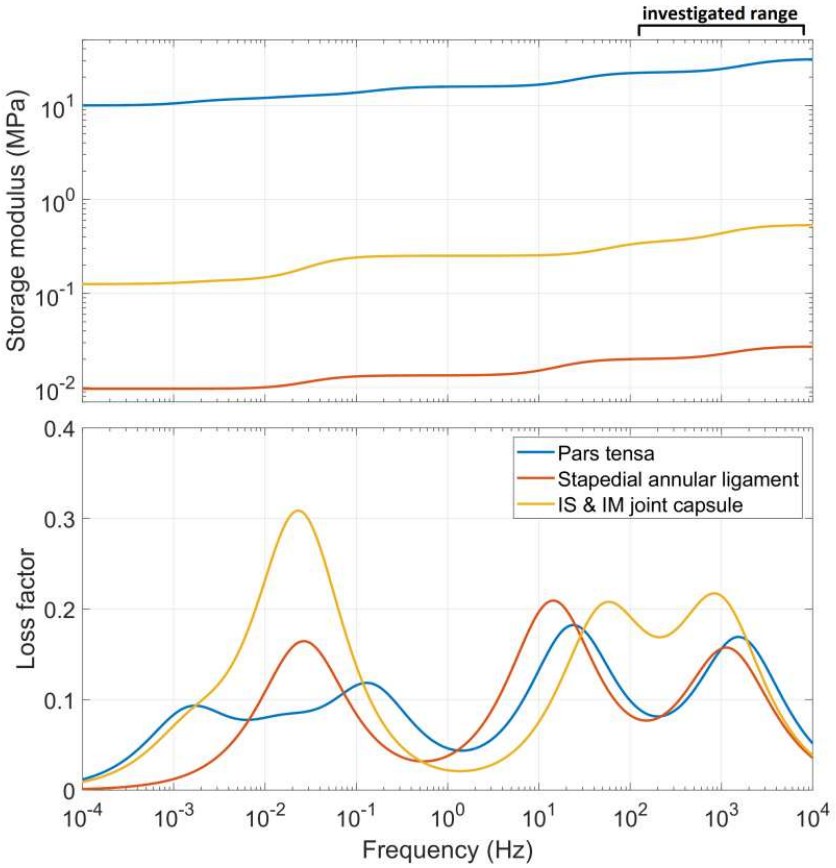

Fig. 7. Shear storage modulus and loss factor of the viscoelastic components used in the FE model. The investigated frequency range for the harmonic simulations is indicated.

For the synovial gaps of the ISJ and IMJ, we approximated the dissipative fluid behavior in the harmonic simulations by defining a viscosity parameter η, which relates the shear stress to the shear rate as $\Delta\mathbf{S}^* = i\omega\eta 2\Delta\boldsymbol{\varepsilon}^*$, with $\Delta\mathbf{S}^*$ the complex amplitude of the infinitesimal deviatoric stress tensor and $\Delta\boldsymbol{\varepsilon}^*$ the complex amplitude of the infinitesimal deviatoric strain tensor. Synovial fluid is a shear-thinning non-Newtonian fluid (e.g., Fam et al., 2007), of which the steady-state viscosity decreases with shear rate, and the dynamic viscosity decreases with frequency. Human synovial fluid has shown viscoelastic behavior in oscillatory shear experiments, which has been described by viscoelastic models (e.g., Lai et al., 1978). However, mechanical rheometry of synovial fluid is currently limited to long time scales or low frequencies. Therefore, it is impossible to construct a viscoelastic model for synovial fluid based on experimental data in the auditory frequency range (Soleimani et al., 2020). In the current model, we used a real-valued viscosity of η = 10 Pa s that was constant with frequency. This value lies in the range of viscosity measurements for normal human synovial fluid in the limit of zero shear rate (12.614 Pa s in Zeidler et al., 1979; 9.56–33.55 Pa s in Safari et al., 1990; 6–12 Pa s in Schurz, 1996; 2.5–100 Pa s in Bingöl et al., 2010). The elastic shear moduli of the synovial gaps in Table 1 were considered to be constant as a function of frequency.

For the remaining components in the model of which no viscous or viscoelastic data was available, we made use of Rayleigh damping, except for the three ossicles which exhibited no damping. For Rayleigh damping, the damping matrix is given by $C = \alpha M + \beta K$, with M and K the mass and stiffness matrices, and α and β damping parameters. We used $\alpha = 0$ s^{-1} and $\beta = 1{\cdot}10^{-4}$ s as in our previous model of the human ME (De Greef et al., 2017). The corresponding elastic parameters were considered as constant with frequency.

For the mass density of the bony ossicles we used the values from our previous FE model, that is, 2390 kg/m^3 for the malleus, 2150 kg/m^3 for the incus, and 2200 kg/m^3 for the stapes (De Greef et al., 2017). For all soft-tissue structures, we used a mass density of 1100 kg/m^3 as in Maftoon et al. (2015).

2.6 Small harmonic motion under large static predeformation

The static simulations in the current work describe the long-term static deformation behavior of the ME at static equilibrium, which is obtained in the limit $t \to \infty$ when all transient stresses and strains upon applying a static load have been relaxed. Possible transient phenomena induced by sudden or slow pressure variations, such as stress relaxation, creep and hysteresis, are therefore disregarded in the static simulations. The dynamic behavior of the ME is represented by steady-state harmonic vibrations induced by small sinusoidal pressure loads, which act as a linear perturbation on top of the static preload. The harmonic motions are small enough to consider the system as linear, so the behavior can be represented by the theory of linear viscoelasticity as described in Section 2.5. To set up the prestressed harmonic simulations, the hyperelastic constitutive equation of the predeformed material is first linearized around the static predeformed state. Starting from this linearized constitutive equation, the harmonic steady-state response of the material under static predeformation is calculated in the frequency domain. In this procedure, the total stress in the material is split into a static prestress part related to the static predeformation and an infinitesimal dynamic part associated with the harmonic motion. For incompressible visco-hyperelastic materials, the linearized constitutive equation for the harmonic motion around a static predeformed state can be characterized in the frequency domain by the relation

$$\Delta\mathbf{S}^* = \left(1 + i\omega g^*(\omega)\right)\mathbb{C}|_{\mathbf{E}_0} : \Delta\boldsymbol{\varepsilon}^*. \tag{13}$$

In this expression, $\Delta\mathbf{S}^*$ is the complex amplitude of the deviatoric part of the infinitesimal stress tensor caused by incremental straining of the material, $\Delta\boldsymbol{\varepsilon}^*$ is the complex amplitude of the infinitesimal deviatoric strain tensor, and $\mathbb{C}|_{\mathbf{E}_0}$ is the fourth-order elasticity tensor of the material linearized around the predeformed strain state $\mathbf{E}_0$, which is derived from the hyperelastic constitutive model (Morman and Nagtegaal, 1983; Kim and Youn, 2001; Lion et al., 2009). The function $g^*(\omega)$ represents the Fourier transform of the nondimensional viscoelastic shear

relaxation function $g(t)$ defined in Eqs. (9–10), which introduces a complex harmonic contribution to $\mathbb{C}|_{\mathbf{E}_0}$. In Eq. (13) we observe that frequency and strain effects are separated in the viscoelastic constitutive relation, which is a fair assumption for many materials. No viscoelastic contribution was considered for the volumetric part of the stress, so viscoelasticity is only produced by shear deformation.

When the above description is implemented in a FE formulation, the static prestress part and the infinitesimal dynamic part of the total stress have separate contributions to the global stiffness matrix K of the preloaded solid, and are denoted the geometric stiffness matrix and linear stiffness matrix, respectively (Morman and Nagtegaal, 1983). As a result, the structural stiffening experienced by a preloaded solid under dynamic excitation is determined by (1) the change of the linearized constitutive relation of the hyperelastic material with the predeformation state, i.e., the material nonlinearity, (2) the prestress in the solid as a result of the static preload, and (3) the geometric configuration of the solid in the deformed state relative to the undeformed state.

To quantify the effect of the material nonlinearity on the change in ME vibration response, we developed a model in which the Veronda–Westmann strain-energy function in Eq. (2) was replaced by the shear term of the Saint–Venant Kirchhoff strain-energy function $\mu\mathbf{E}:\mathbf{E}$, which assumes a linear relationship between the second Piola-Kirchhoff stress $\mathbf{S}$ and Green-Lagrange strain $\mathbf{E}$. This substitution was applied to all hyperelastic components, but only for the harmonic perturbation and not the static predeformation simulations. In this way, the harmonic response was calculated around the predeformed state of the base model. These additional simulations are referred to as *linear elasticity* in the results. By considering the difference between the linear elasticity simulations and the *full model* (i.e., the base model with all structural stiffening mechanisms included), the effect of material nonlinearity on the preloaded harmonic response can be evaluated.

To quantify the additional effect of removing the pressure-induced prestress and prestrain on the vibration response, we exported the deformed geometry resulting from the static simulations of the base model and used it as initial geometry for separate harmonic simulations. In this way, the prestress and prestrain built up in the solid due to the static preload are disregarded. Therefore, these simulations only consider the effect of the deformed geometry on the vibration response and ignore the effect of pressure-induced prestress and material nonlinearity. These simulations are referred to as *deformed geometry only* in the results. By considering the difference between the deformed geometry only model and the linear elasticity model, the effect of the pressure-induced prestress on the preloaded harmonic response can be determined. On the other hand, by considering the difference between the deformed geometry only model and the base model without static preload, the effect of the deformed geometry on the preloaded harmonic response can be evaluated.

2.7 Sensitivity analysis

Because of the uncertainty on the elastic parameter values, we performed a sensitivity analysis to estimate the relative effects of the parameters on the base model. In this procedure, we varied the parameters in Table 1 by factors 2 and 1/2 and investigated the effect on (1) the stapes footplate velocity magnitude in the absence of static preload, (2) the footplate velocity change under a static preload of +1 kPa, and (3) the footplate velocity change under a preload of –1 kPa. To minimize the number of calculations, we divided the ME components into several groups by varying their parameters simultaneously. These groups consisted of the ossicles (malleus, incus and stapes), the TM components (PT, PF, TMC and TA), the ligaments and tendons attached to the ossicles (SMT, TTT, AML, LML, SML and PIL), the joint capsules (IMJ and ISJ), the joint cartilage layers (IMJ and ISJ), the joint synovial gaps (IMJ and ISJ) and the SAL, which was considered a separate group. We performed the calculations at three selected frequencies of 0.125 kHz (low), 1 kHz (mid) and 8 kHz (high). Because the variations were applied to each group individually, we did not account for the effect of parameter interactions that may occur when different groups of parameters are varied together.

Because it is not well understood how the mechanical properties of the joints affect ME sound conduction, we did a separate sensitivity analysis on the parameters of the joints. In this procedure, we examined the effect of varying the long-term elastic and viscoelastic base parameters of the IMJ and ISJ components by factors 10 and 1/10 on the ME vibration response. We varied the parameters μ, b and g_i (for all i simultaneously) of the ISJ and IMJ capsule, μ and η of the IMJ and ISJ synovial gap, and E and β of the IMJ and ISJ cartilage layers. With these parameter variations, we evaluated the effect on the umbo and footplate velocity magnitude without preload and the footplate velocity change under preloads of +1 and –1 kPa. In this analysis, the response was calculated over the entire frequency range of 0.125–8 kHz.

2.8 Computational specifications

The FE calculations were performed on a desktop computer (Intel(R) Xeon(R) CPU E5-2630 v3, 2.40 GHz (2 processors), and 128 GB of RAM). The final FE model consisted of ~250,000 degrees of freedom. The computation time for the static simulations of the base model was about 13–14 min in the pressure range of 0 to +4 or –4 kPa when using pressure steps of 0.1 kPa. For the harmonic simulations of the base model, the computation time was ~14 min over the frequency range of 0.125–8 kHz, evaluated at eight frequencies per octave.

3. Results

3.1 Long-term static analysis

Fig. 8 shows the simulated static out-of-plane displacements of the umbo (top) and stapes footplate (bottom) as a function of static ear-canal pressure, compared to the experimental data of Hüttenbrink (1988), Murakami et al. (1997) and Dirckx and Decraemer (1991). In the bottom panel, a small panel was added showing the umbo-to-footplate displacement ratio (in dB). The results are shown for the base model with hyperelastic Veronda–Westmann parameters and an adapted model with linear elastic properties that considers only geometric nonlinearity.

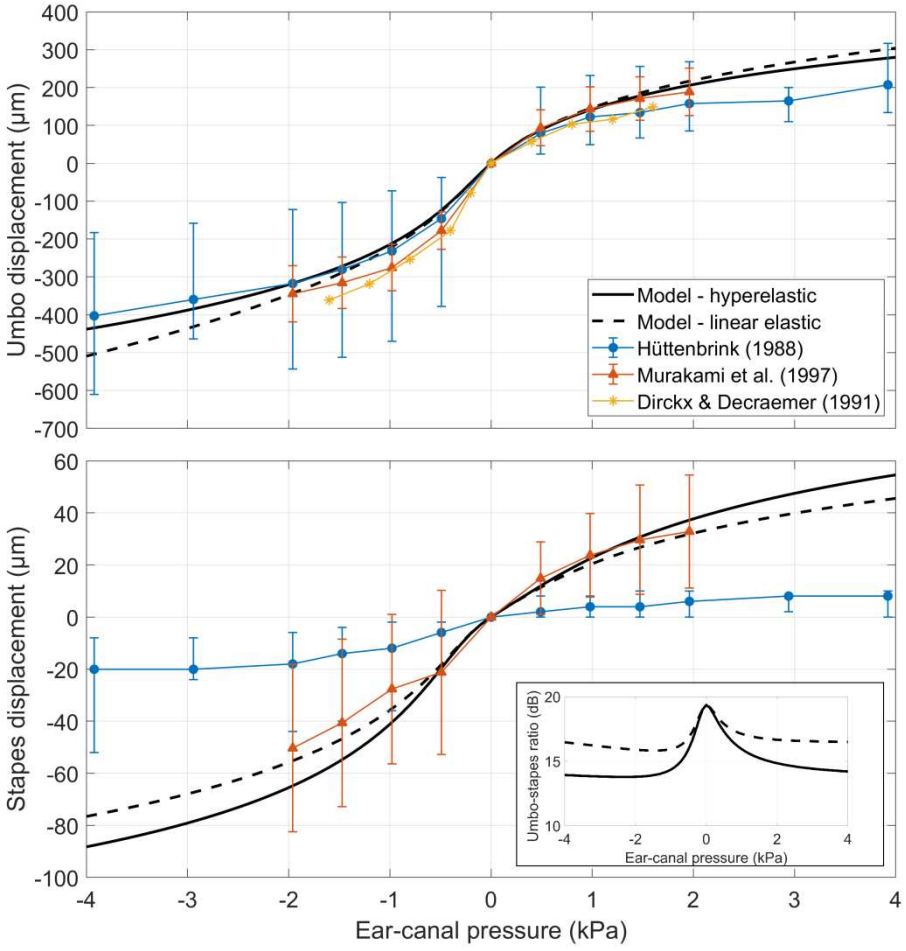

Fig. 8. Static out-of-plane displacement of the umbo and stapes footplate as a function of ear-canal pressure, comparing the model results to experimental data. Negative (resp. positive) displacements denote movements in the lateral (resp. medial) direction. FE results are shown for the base model with hyperelastic parameters and a modified model with linear elastic parameters. The data of Hüttenbrink denote the median with the total measurement range as error bars. The data of Murakami et al. (1997) show the mean with the standard deviation as error bars. The umbo data of Dirckx and Decraemer (1991) are from a single measurement. The small panel in the bottom panel depicts the umbo-to-footplate displacement ratio (in dB).

The displacement curves of the base model with hyperelastic material properties show an asymmetric nonlinear S-shape, with higher displacements for negative than positive pressure. The umbo displacement at negative pressure shows the best match with the median result of Hüttenbrink (1988), while at positive pressure the agreement is best with the mean of Murakami et al. (1997). For the stapes, the overall agreement is better with the data of Murakami et al. (1997), which show larger displacements than the data of Hüttenbrink (1988). When the Veronda-Westmann parameters are replaced by linear elastic ones, the absolute umbo displacements show an increase with static pressure, which is most pronounced at negative pressure. For the stapes, the displacements of the linear elastic model decrease relative to the hyperelastic model, which is the case for both negative and positive pressure. The hyperelastic and linear elastic model both fall within the measurement range. The umbo-to-footplate ratio amounts to 19 dB (linear ratio of 9) in the limit of zero static pressure, and decreases as a function of static pressure to 14 dB (linear ratio of 5) for the hyperelastic model and to 16.5 dB (linear ratio of 6.7) for the linear elastic model.

3.2 Harmonic analysis

3.2.1 Harmonic response without static predeformation

Fig. 9 shows the simulated harmonic velocity response of the ME (magnitude, phase and magnitude ratio), evaluated at the umbo and stapes footplate. We compare the simulated footplate data to ranges of measurement data presented in the literature; the magnitude is compared to the range of the experimental standard for the normalized footplate velocity (ASTM Standard F2504-05, 2014), and the phase is compared to the data range of Aibara et al. (2001), both comprising two standard deviations. In addition, the magnitude and phase are compared to five selected individual measurements of Aibara et al. (2001). The umbo-to-footplate magnitude ratio is compared to experiments of Gan et al. (2004), Nishihara et al. (1993) and Kurokawa et al. (1995). The simulated response is depicted for two situations: one curve shows the base-model response with a viscoelastic characterization for the PT, SAL, and joint capsules (solid lines); the other curve shows the model response when a Rayleigh-damping characterization is used for these components instead, with constant elasticity parameters as a function of frequency (dashed lines).

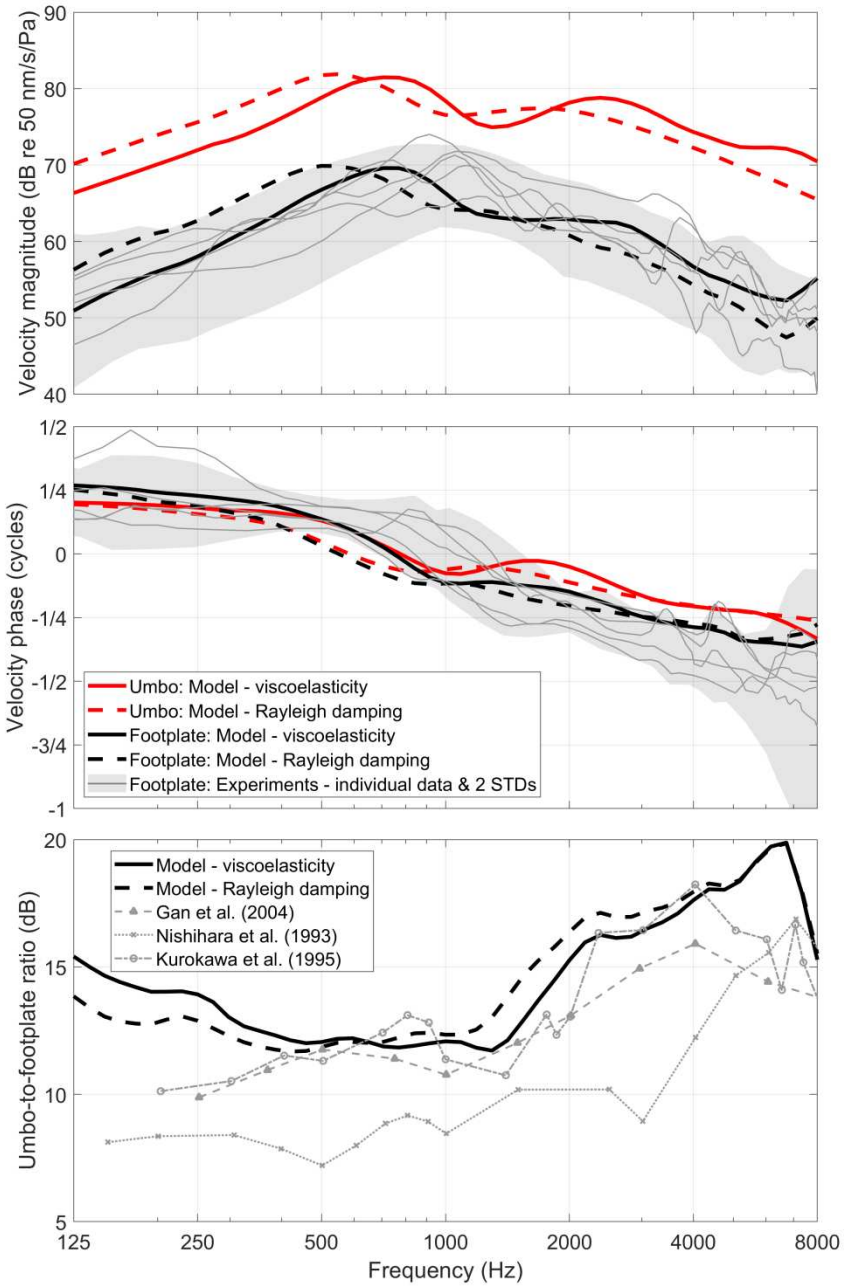

Fig. 9. Harmonic out-of-plane velocity response (magnitude, phase and magnitude ratio) of the umbo and stapes footplate, comparing the model to experimental footplate data. The range of the gray bands for the experimental data (magnitude: ASTM Standard F2504-05, 2014; phase: Aibara et al., 2001) represents 95% confidence levels or two standard deviations. The individual magnitude and phase curves are measurements of Aibara et al. (2001). In the Rayleigh-damping model (dashed lines), the viscoelastic description of the PT, SAL and joint capsules in the base model (full lines) was replaced by a Rayleigh-damping description with $\beta = 1{\cdot}10^{-4}$ s.

The footplate response of the viscoelastic model shows a better agreement with the measurements than the Rayleigh-damping model. First of all, the viscoelastic model depicts a more realistic low-frequency response below 0.5 kHz than the model with only Rayleigh damping. Secondly, the resonance frequency of the

viscoelastic model (0.77 kHz), which we define as the frequency where the velocity phase equals 0, falls within the range of individual curves included in the experimental data (~0.7–1.4 kHz). The resonance frequency of the Rayleigh-damping model (0.55 kHz) falls outside this range, although the difference with the viscoelastic model only amounts to 0.22 kHz. Finally, the degree of high-frequency fluctuations of the viscoelastic model is more comparable to the fluctuations found in individual experimental curves than the fluctuations of the Rayleigh-damping model, although the experimental curves still show stronger fluctuations. The Rayleigh-damping model, however, is slightly closer to the mean of the experimental magnitude range than the viscoelastic model. In both models, the umbo response shows a similar behavior as the footplate response as a function of frequency. However, the umbo magnitude is about 12–20 dB higher than the footplate magnitude, and the umbo phase degrades slightly slower with frequency. The umbo-to-footplate ratio decreases slowly from 15 dB at 0.125 kHz to 12 dB at 1.3 kHz, and then increases considerably up to 20 dB at 7 kHz, after which it drops to 15 dB at 8 kHz. The increase above 1.3 kHz and the subsequent drop at high frequencies is similar to the experimental observations, and shows the best agreement with the data of Nishihara et al. (1993). The slow decrease starting at 0.125 kHz is not observed experimentally.

3.2.2 Harmonic response with static predeformation

Fig. 10 shows the changes in umbo (top) and footplate (bottom) vibration magnitude relative to the unloaded condition for different positive ear-canal pressures (+0.5, +1, +2 and +4 kPa) (left), and negative ear-canal pressures (–0.5, –1, –2 and –4 kPa) (right). The results of the base model are compared to the mean experimental data of Murakami et al. (1997), Gan et al. (2006) and Homma et al. (2010). We remark that Gan et al. (2006) made their footplate measurements with an opened cochlea. This approach differs from the other experiments and our model, which were obtained with an intact cochlear load.

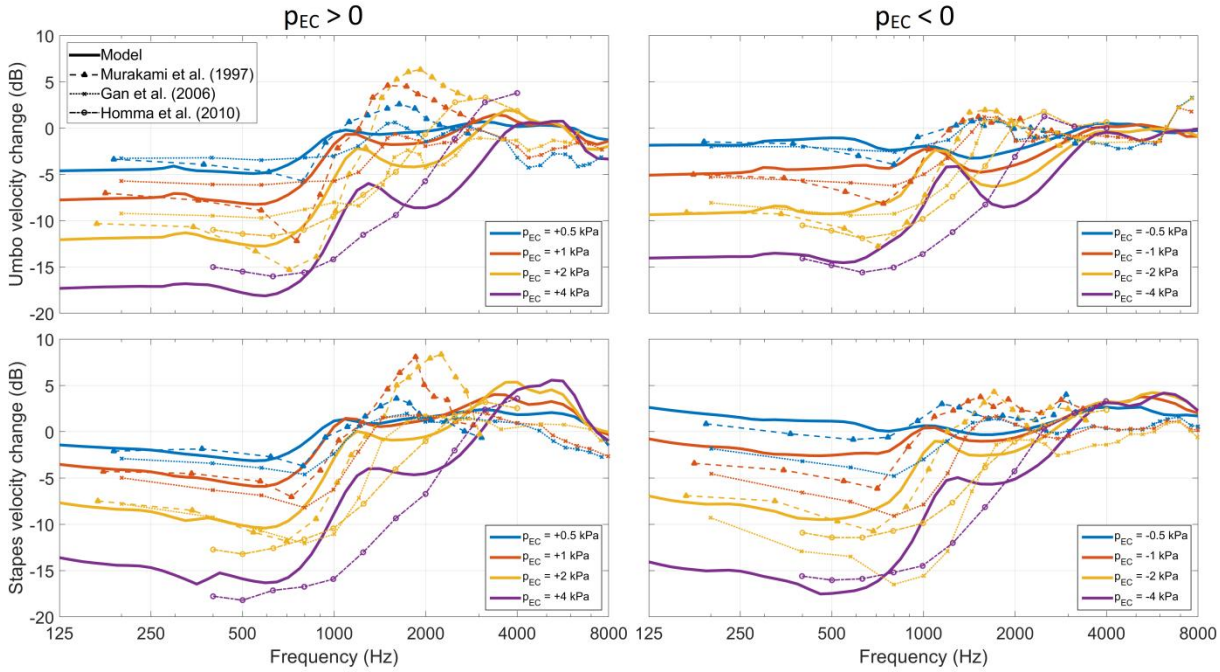

Fig. 10. Change in umbo and stapes footplate vibration magnitude relative to the unloaded condition at (left) positive static ear-canal pressures p_{EC} (+0.5, +1, +2 and +4 kPa), and (right) negative static ear-canal pressures p_{EC} (–0.5, –1, –2 and –4 kPa). The results from the base model are compared to the averages of measurements from Murakami et al. (1997), Gan et al. (2006) and Homma et al. (2010).

From Fig. 10, it can be deduced that the umbo and footplate response decrease with increasing positive or negative pressure at frequencies below 1 kHz; the transition frequency between the observed low- and high-frequency behavior is somewhat lower than in most of the experiments. At high frequencies above 2 kHz, the changes in umbo and footplate response are closer to 0 dB; for the footplate, the model shows an increase above 0 dB at some frequencies. The decrease below 1 kHz for the umbo shows a plateau, with a local dip between 0.5 and 1 kHz found especially at positive static pressures. The low-frequency plateau for the footplate shows a gradual decline by 2.5 dB from 0.125 to 0.5 kHz, reaching a minimum between 0.5 and 1 kHz. This behavior is also reflected in the experimental data. The decrease of the umbo response at low frequencies is about 2.5 dB higher for positive than negative pressures. This difference is also present in the experimental data but to a lesser extent. For the footplate, the decrease in vibration response with static pressure accumulates more with increasing negative than increasing positive pressure. This characteristic is also observed in the experiments but to a lesser degree. At a negative pressure of –0.5 kPa, the footplate response shows an increase relative to the unloaded case. Murakami et al. (1997) also observed this behavior in some measurements, but our model shows a clear difference with the combined average of Murakami et al. (1997) and Gan et al. (2006) at –0.5 and –1 kPa, which do not exceed 0 dB.

Fig. 11 shows the change in vibration magnitude of the umbo (top) and footplate (bottom) for positive static pressures (+0.5, +1, +2 & +4 kPa) (left) and negative static pressures (–0.5, –1, –2 & –4 kPa) (right) with different effects of structural stiffening included in the model, as explained in Section 2.6. Solid lines represent the results of the base model with all effects of structural stiffening included (full model). Dashed lines depict the model results without material nonlinearity but including pressure-induced prestress and deformed geometry (linear elasticity). Dotted lines show the model results with only the effect of the deformed geometry included (deformed geometry only).

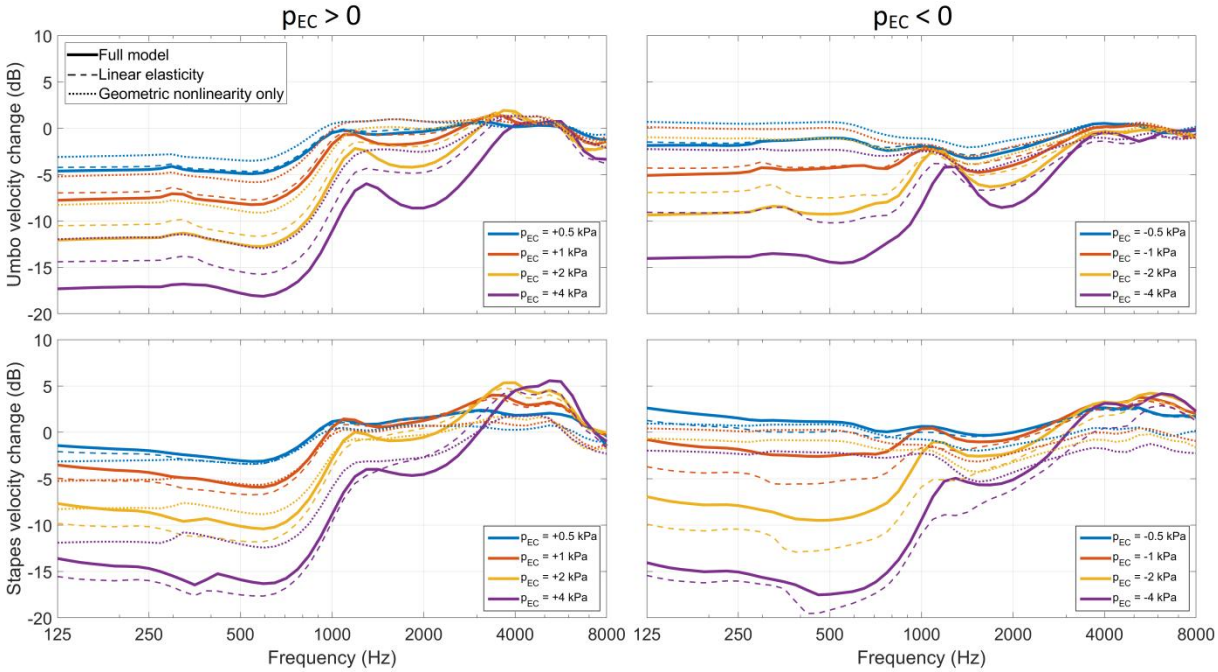

Fig. 11. Simulated change in umbo and stapes footplate vibration magnitude at (left) positive ear-canal pressures p_{EC} (+0.5, +1, +2 and +4 kPa), and (right) negative ear-canal pressures p_{EC} (–0.5, –1, –2 and –4 kPa). The base model including all effects of structural stiffening (full model) is compared to a model without material nonlinearity in which all hyperelastic parameters are replaced by linear elastic ones for the harmonic simulations (linear elasticity), and a model that uses the deformed geometry of the static predeformation as input geometry for the harmonic simulations (deformed geometry only).

For positive pressures in Fig. 11 (left), we observe that the umbo and footplate response of the model with deformed geometry only (dotted lines) decrease at low frequencies relative to the unloaded condition, indicating structural stiffening. When we additionally include the effect of pressure-induced prestress by considering the linear elasticity model (dashed lines), we observe that the umbo response decreases relative to the deformed geometry only model for all static pressures. However, because the difference between the linear elasticity model and the deformed geometry only model is smaller than the difference between the deformed geometry only model and the unloaded case, the stiffening at the umbo due to pressure-induced prestress is smaller than that

caused by the deformed geometry. For the footplate, the response decreases at high pressures (+2 and +4 kPa) but increases at low pressures (+0.5 and +1 kPa) when comparing the linear elasticity to the deformed geometry only result. When finally material nonlinearity is included by considering the full model (solid lines), we observe a reduction of the umbo response relative to the model with linear elasticity. Nevertheless, because the difference between the full model and the linear elasticity model is smaller than the difference between (1) the linear elasticity model and the deformed geometry only model, and (2) the difference between the deformed geometry only model and the unloaded model, the stiffening at the umbo caused by material nonlinearity is smaller than the stiffening caused by the deformed geometry and pressure-induced prestress. For the footplate, we observe an increase at all static pressures when comparing the full model to the linear elastic model, which indicates a situation with less stiffening.

For negative pressures in Fig. 11 (right), the result with deformed geometry only (dotted lines) has a much smaller effect on the umbo and footplate response than for positive pressures. At –0.5 and –1 kPa, there is even a small increase of the low-frequency response or softening relative to the unloaded condition. When we take pressure-induced prestress into account by considering the linear elasticity model (dashed lines), we observe a substantial decrease of the response or stiffening relative to the result with deformed geometry only that accumulates with the static pressure, especially for the footplate. When finally material nonlinearity is incorporated by considering the full model (solid lines), the umbo response decreases relative to the linear elasticity model, especially at –2 and –4 kPa. However, because the difference between the full model and the linear elasticity model is smaller than the difference between the linear elasticity model and the deformed geometry only model, the stiffening at the umbo due to material nonlinearity is smaller than the stiffening due to pressure-induced prestress. The footplate response of the full model, on the other hand, shows an increase relative to the linear elastic case at all static pressures, illustrating a condition with less stiffening.

3.3 Sensitivity analysis

3.3.1 Elastic material properties

Fig. 12 shows the effect of individually varying the elastic material parameters by factors 2 and 1/2 on the footplate vibration response at 0.125 kHz (left), 1 kHz (middle) and 8 kHz (right). The effect is calculated on the velocity magnitude in the absence of static preload (top row), the change in footplate velocity magnitude relative to the unloaded case for a positive static preload of +1 kPa (middle row), and for a negative static preload of –1

kPa (bottom row). The parameters b of the Veronda–Westmann materials were not included in the graphs of the unloaded velocity magnitude (top) because they only affect the response in the presence of static predeformation.

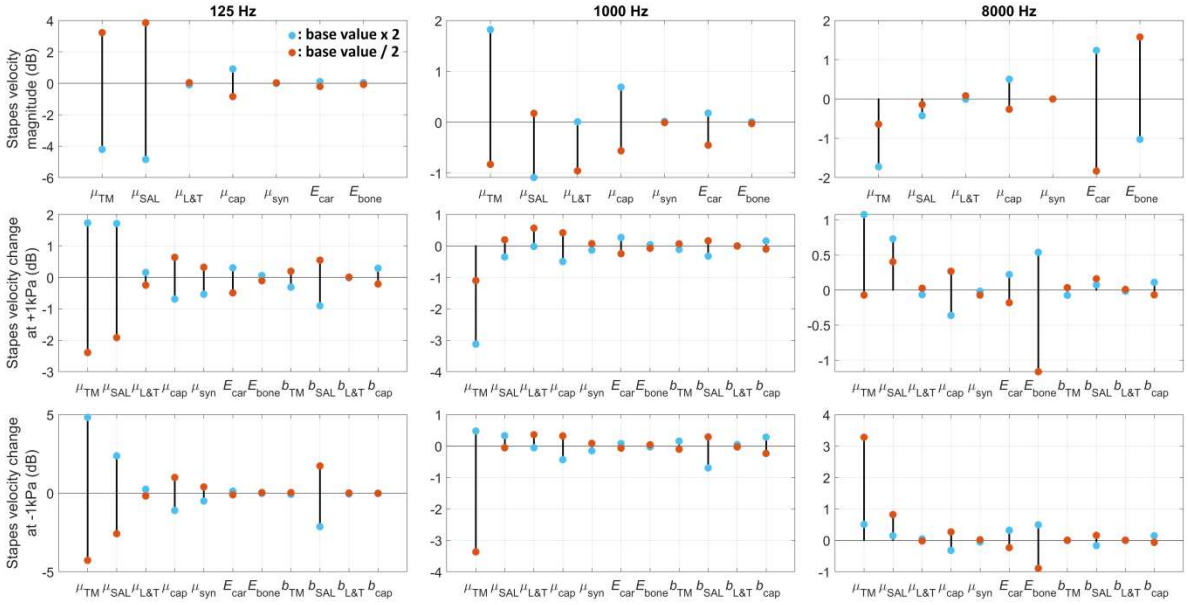

Fig. 12. Effect of individually varying the elastic parameters by factors 2 and 1/2 on the stapes footplate velocity magnitude in the absence of static preload (top row), the change in stapes footplate velocity magnitude relative to the unloaded condition due to a preload of +1 kPa (middle row), and a preload of −1 kPa (bottom row). The effects are evaluated at 0.125 kHz (left), 1 kHz (middle) and 8 kHz (right). TM, tympanic membrane (PT, PF, TMC and TMA); SAL, stapedial annular ligament; L&T, ligaments and tendons (SMT, TTT, AML, LML, SML and PIL); cap, IMJ and ISJ capsule; syn, IMJ and ISJ synovial gap; car, IMJ and ISJ cartilage; bone, bony ossicles (malleus, incus and stapes). μ, shear modulus at zero strain; E, Young's modulus; b, hyperelastic Veronda-Westmann parameter.

In Fig. 12 (top row), we observe that μ_{SAL} and μ_{TM} have the highest effect at 0.125 kHz. At 1 kHz, the effect of μ_{TM} is highest. At 8 kHz, μ_{TM}, E_{car}, and E_{bone} have the highest effects. At 0.125 kHz, increasing μ_{TM} and μ_{SAL} leads to a decrease in the response, while increasing μ_{cap} and E_{car} leads to an increase, also at higher frequencies. The shear modulus μ_{cap} has more impact at low and mid frequencies, whereas E_{car} has more impact at mid and high frequencies. At 1 kHz, increasing μ_{TM} leads to an increase as opposed a decrease at 0.125 kHz, which indicates a shift of the resonance frequency to higher frequencies. The shear modulus $\mu_{\mathrm{L\&T}}$ only has a noticeable effect at 1 kHz, while E_{bone} of the ossicles only affects the response at 8 kHz. The parameter μ_{syn} has almost no effect on the footplate magnitude.

In Fig. 12 (middle row), μ_{TM} has the highest effect at 0.125 kHz and 1 kHz, while E_{bone} has the highest effect at 8 kHz. At 0.125 kHz, μ_{SAL} has the second-to-highest effect. We notice that increasing μ_{TM} and μ_{SAL}

leads to a positive variation of the velocity change, which means that the reduction of the footplate response relative to the unloaded case is smaller than in the base model. The effect of μ_{cap} and μ_{syn} of the joints is opposite to that of μ_{TM} and μ_{SAL}, while the effect of E_{car} shows the same polarity as μ_{TM} and μ_{SAL}. Also the parameter b_{SAL} has a strong influence. Increasing b_{TM} and b_{SAL} leads to a negative variation of the velocity change, which means that the reduction of the stapes response relative to the unloaded case is higher than in the base model. At 1 kHz, the second-to-highest effect behind μ_{TM} is caused by μ_{SAL} and μ_{cap}. At 8 kHz, E_{bone} has a considerable effect. At 1 kHz, increasing and decreasing μ_{TM} both lead to a negative variation of the velocity change, indicating that the reduction of the footplate response relative to the unloaded case is higher than in the base model. For the hyperelastic parameters b, the effect is typically lower than for the shear moduli μ at all frequencies. The effect of $b_{\mathrm{L\&T}}$ is almost negligible.

In Fig. 12 (bottom row), we observe that μ_{TM} has the highest effect for all frequencies. At 0.125 kHz, μ_{SAL} and b_{SAL} have the second-to-highest effect. Similar to the results at positive pressure, increasing μ_{TM}, μ_{SAL} and E_{car} leads to a positive variation of the velocity change, while increasing μ_{cap}, μ_{syn} and b_{SAL} has the opposite effect. At 1 kHz, multiple parameters have a considerable impact on the velocity change beside μ_{TM}, namely μ_{SAL}, $\mu_{\mathrm{L\&T}}$, μ_{cap}, b_{SAL} and b_{cap}. At 8 kHz, the shear moduli μ and Young's moduli E have a small but noticeable effect, while the parameters b have very little effect.

3.3.2 Viscoelastic properties of the joints

Fig. 13 shows the effect of the varying the base parameters μ, b and g_i of the capsule of the IMJ (left) and ISJ (right) by factors 10 and 1/10 on the ME vibration response. The effect is shown for the umbo and footplate velocity magnitude without preload (top), and the footplate velocity change relative to the unloaded case due to a preload of +1 kPa (middle) and −1 kPa (bottom).

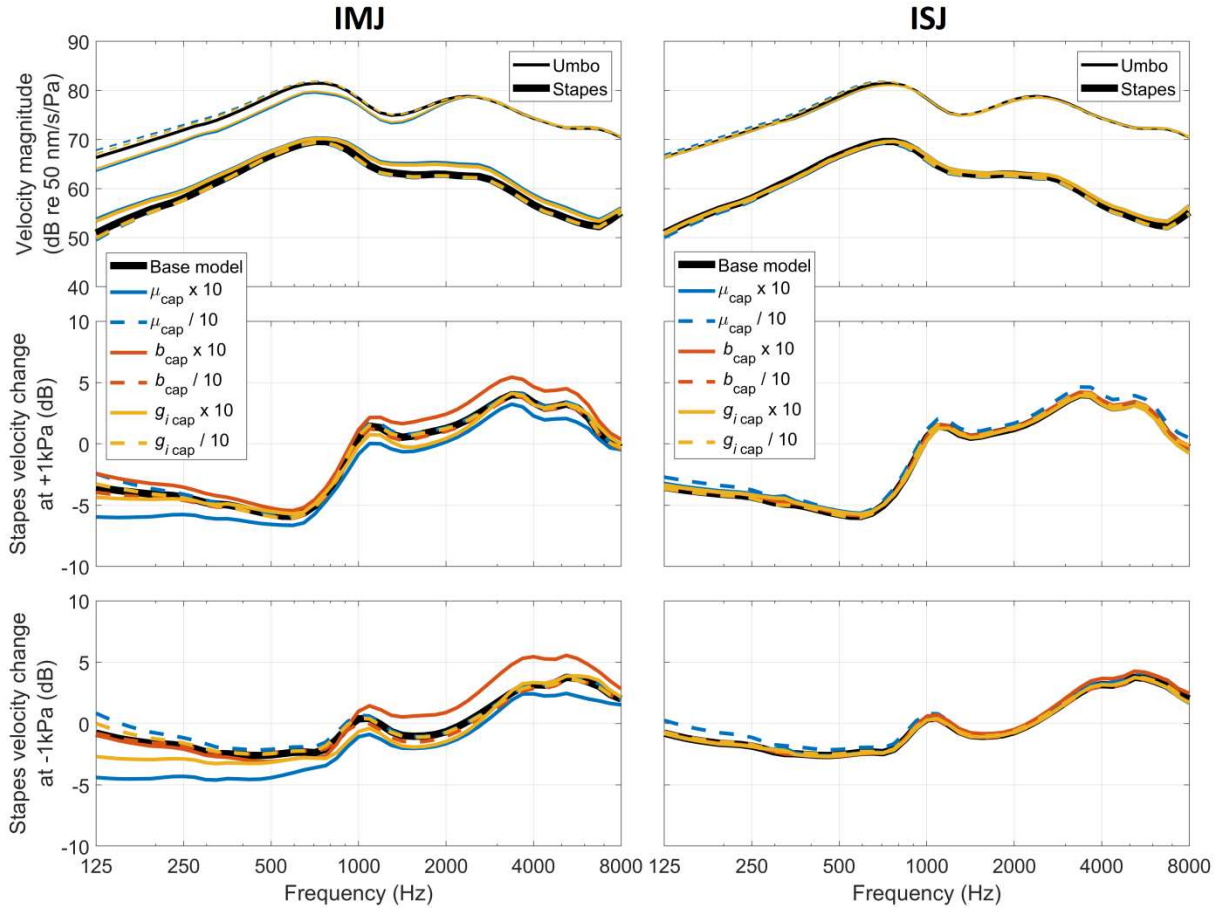

Fig. 13. Effect of varying the base parameters of the capsule of the IMJ (left) and ISJ (right) by factors 10 and 1/10 on the umbo and stapes footplate velocity magnitude without preload (top), and the footplate velocity change relative to the unloaded condition due to a preload of +1 kPa (middle) and –1 kPa (bottom). μ, shear modulus at zero strain; b, hyperelastic Veronda-Westmann parameter; g_i, shear relaxation coefficients.

In Fig. 13 (left, top panel), it can be seen that increasing μ_{cap} by a factor 10 for the IMJ reduces the gap between the umbo and footplate vibration magnitude. Increasing $g_{i_{\text{cap}}}$ for the IMJ has a similar effect, which was to be expected because increasing $g_{i_{\text{cap}}}$ leads to an increase of the storage modulus G', just like increasing μ_{cap} does. Varying μ_{cap} and $g_{i_{\text{cap}}}$ by a factor 1/10 instead increases the umbo-to-footplate ratio, but by a smaller amount than the decrease observed for the variation by a factor 10. In Fig. 13 (left, middle and bottom panels) we see that increasing μ_{cap} and $g_{i_{\text{cap}}}$ causes a reduction of the footplate velocity change relative to the unloaded case. Increasing b_{cap} raises the footplate velocity change curves by a small amount, and mostly at high frequencies. The effects of the parameters of the ISJ capsule (Fig. 13 (right)) are almost invisible; decreasing μ_{cap} by a factor 10 affects the umbo and footplate magnitudes and the footplate velocity change curves by maximally 1 dB.

Fig. 14 shows the effect of the varying the base parameters μ and η of the synovial gap of the IMJ (left) and ISJ (right) by factors 10 and 1/10. The resulting effect is depicted for the umbo and footplate velocity magnitude without preload (top), and the footplate velocity change relative to the unloaded case due to a preload of +1 kPa (middle) and −1 kPa (bottom).

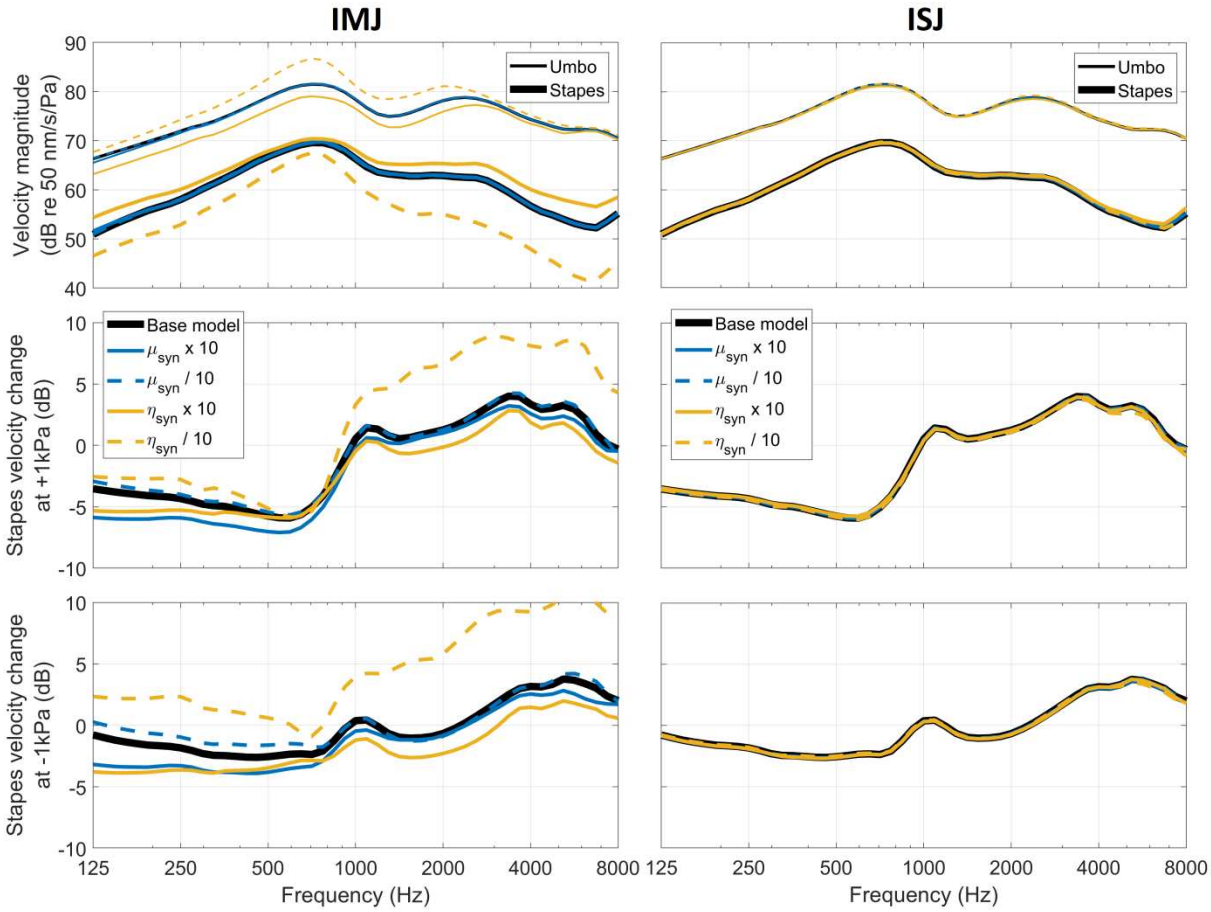

Fig. 14. Effect of varying the base parameters of the synovial gap of the IMJ (left) and ISJ (right) by factors 10 and 1/10 on the umbo and stapes footplate velocity magnitude without preload (top), and the footplate velocity change relative to the unloaded condition due to a preload of +1 kPa (middle) and −1 kPa (bottom). μ, shear modulus at zero strain; η, viscosity.

In Fig. 14 (left, top panel), we see that decreasing η_{syn} of the IMJ drastically increases the gap between the umbo and footplate response, while increasing η_{syn} brings the curves closer together. Decreasing η_{syn} raises the curves of the footplate velocity change (Fig. 14, left, middle and bottom panels). Increasing η_{syn} has the opposite effect on the velocity change curves, but with a smaller impact. Varying μ_{syn} has a negligible effect on the velocity magnitude (Fig. 14, left, top panel), although increasing μ_{syn} causes a further reduction of the footplate change curves (Fig. 14, left, middle and bottom panel). The synovial-gap parameters of the ISJ (Fig. 14 (right)) have almost no effect.

Fig. 15 shows the effect of the varying the base parameters E and β of the cartilage layers of the IMJ (left) and ISJ (right) by factors 10 and 1/10. The resulting effect is depicted for the umbo and footplate velocity magnitude without preload (top), and the footplate velocity change relative to the unloaded case due to a preload of +1 kPa (middle) and –1 kPa (bottom).

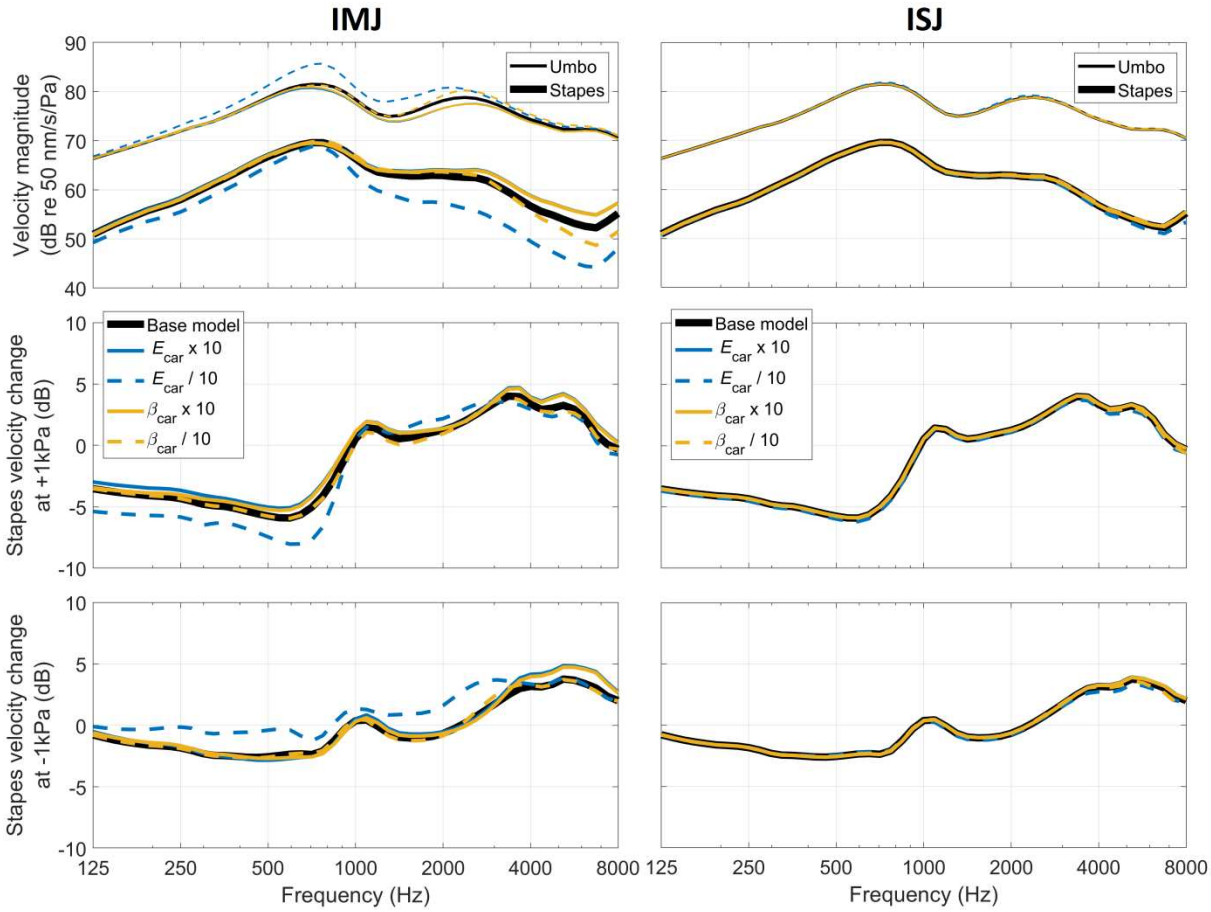

Fig. 15. Effect of varying the base parameters of the cartilage layers of the IMJ (left) and ISJ (right) by factors 10 and 1/10 on the umbo and stapes footplate velocity magnitude without preload (top), and the footplate velocity change relative to the unloaded condition due to a preload of +1 kPa (middle) and –1 kPa (bottom). E, Young's modulus; β, Rayleigh damping coefficient.

In Fig. 15 (left, top panel), we observe that decreasing E_{car} of the IMJ increases the gap between the umbo and footplate response, while increasing E_{car} has a smaller and opposite effect. At low frequencies, we see that decreasing E_{car} further reduces the velocity change curve for positive pressure (Fig. 15, left, middle panel), but increases the curve for negative pressure (Fig. 15, left, bottom panel). Varying β_{car} has a much smaller effect on the velocity changes, although increasing β_{car} reduces the umbo-to-footplate ratio at mid and high frequencies. The parameters of the cartilage layers of the ISJ (Fig. 15 (right)) have no noticeable effect.

4. Discussion

4.1 Static behavior

In Fig. 8, we examined the static displacements of the umbo and footplate due to static ear-canal pressures up to –4 and +4 kPa. The differences between the linear and hyperelastic model were found to be relatively small (up to 17% for both umbo and stapes). Therefore, geometric nonlinearity seems to have more impact on the static behavior than material nonlinearity. Nevertheless, material nonlinearity becomes increasingly relevant at high static pressures, especially under negative pressure. Upon investigation, the differences between the linear and hyperelastic model at negative pressure are affected the most by material nonlinearity of the IMJ capsule, both at the umbo (for 60%) and footplate (for 30%). At positive pressures, the differences due to material nonlinearity at the umbo are influenced the most by the TM (for 67%), and the differences at the stapes are affected the most by the IMJ capsule (for 73%).

According to the findings of Wang et al. (2007), Ihrle et al. (2013) and Zhang et al. (2020), the static displacement asymmetry between positive and negative pressure is mainly a result of the TM geometry. Under positive ear-canal pressure, the inward conical TM is pushed further inward, causing the TM to be stretched. In other words, the static deformations are impeded by the high in-plane stiffness of the membrane. Under negative ear-canal pressure, the TM is pulled outward, causing the membrane to slacken without being impeded by its in-plane stiffness. An opposite asymmetry has been observed in the bird ME of chickens, which have outward conical TMs (Muyshondt et al., 2019).

4.2 Harmonic response without static preload

In Fig. 9, we evaluated the velocity magnitude of the umbo and footplate under zero static pressure for a model with viscoelastic parameters for the PT, SAL and joint capsules, and a model with Rayleigh damping for all soft-tissue structures. It was shown that viscoelasticity is needed to obtain a realistic low-frequency response and resonance frequency (0.77 kHz), considering the observation that viscoelasticity causes an increase of the storage modulus with frequency (see Fig. 7 (top)). When instead the storage modulus is chosen equal to the static elastic modulus as in the Rayleigh-damping model, the dynamic stiffness decreases, causing a shift of the frequency response to lower frequencies by 0.22 kHz (Fig. 9). By replacing the viscoelastic description of the TM, SAL and joints by a Rayleigh-damping description for the different components individually, we found that the viscoelasticity of the TM is most responsible for the change of the resonance frequency (for 54%). Although it was not the objective of the present model to match the characteristics of an average footplate response, the

resonance frequency of the model (0.77 kHz) was slightly lower than average (~1 kHz). Despite that our resonance frequency fell within the range of experimental data, the small observed offset might be due to the fact that the viscoelastic characterization of the ME is not complete; the relaxation coefficients g_i might be underestimated, the number of viscoelastic branches might be insufficient (there could be important branches in the range between short and long time scales (0.01–1 s) for which no viscoelastic data was available), or viscoelasticity of components other than the TM, SAL and joint capsules might be relevant.

The harmonic behavior of the human ME has been investigated together with the static behavior in different numerical studies. In Wang et al. (2007) and Ihrle et al. (2013), the resonance frequency of the harmonic footplate response was closer to the average of experimental data (~1 kHz) than in our study. These studies, however, did not consider the viscoelastic variation of the material parameters with frequency. Instead, the base values of the dynamic elastic moduli (used in the harmonic simulations) were defined independently of the long-term elastic moduli (used in the static simulations) to optimize the ME response function. There is, however, no physical basis for such an approach. In Zhang et al. (2020), a footplate response was obtained with a lower resonance frequency than in our work (~0.6 kHz for a displacement phase of –90°). Similar to our study, Zhang et al. (2020) considered viscoelastic material parameters and used frequency-dependent storage moduli that depended on the long-term static elastic moduli. However, they modeled viscoelasticity by a standard linear solid obtained from another FE model (Zhang and Gan, 2013b). Because a standard linear solid contains only a single viscoelastic branch, the variation of material stiffness and damping with frequency might be described incompletely.

4.3 Structural stiffening of harmonic response under preload

Different studies have used FE modeling to investigate the changes in the sound-induced ME behavior under static pressure (Wang et al., 2007; Homma et al., 2010; Zhang and Gan, 2013b; Ihrle et al., 2013; Sackmann et al., 2019; Zhang et al., 2020). Wang et al. (2007) and Zhang and Gan (2013b) accounted for material nonlinearity by defining dynamic moduli that varied with the static stress. In their model, the stress dependence of the dynamic moduli was simulated by an empirical correction to the stress dependence of the static moduli, which was based on experimental stress-strain data. The base values of the dynamic elastic moduli under stress-free conditions, however, were defined independently of the static moduli. Similar to our study they took into account the effect of the deformed geometry but they ignored the prestress due to static preload. Homma et al. (2010) simulated structural stiffening due to static preload by manually adjusting the dynamic elastic moduli until they obtained a good match with dynamic data under static preload. With their approach, however, it was

impossible to discriminate between the underlying effects of structural stiffening. To incorporate the effect of material nonlinearity on ME structural stiffening, Ihrle et al. (2013) and Sackmann et al. (2019) simulated the dynamic elastic modulus of the TM by a stress-dependent tangent modulus $d\sigma/d\varepsilon = a\sigma + b$, in which σ is the static stress, a a stiffening characteristic derived from uniaxial stress-strain data, and b the elastic modulus in the unloaded case. The parameter b was defined independently of the static model but chosen to match experimental transfer behavior of the ME. In their simulations, they incorporated the effect of the deformed geometry but did not report on the effect of the pressure-induced prestress. Zhang et al. (2020) used a similar approach to ours to model preloaded harmonic ME behavior, although they simulated hyperelasticity by an incompressible first-order Ogden model and viscoelasticity by a standard linear solid. Zhang et al. (2020) did not investigate the relative importance of the underlying mechanisms contributing to structural stiffening.

In Fig. 10 and the second paragraph of Section 3.2.2, we compared our model results of the change in ME vibration response under static pressure with experimental data (Murakami et al., 1997; Gan et al., 2006; Homma et al., 2010). At low frequencies, we observed a decrease of the umbo and footplate response below the resonance frequency, and at high frequencies we found a small increase of up to 6 dB in some cases. This behavior is in agreement with measurements of the hearing threshold under static pressure (von Békésy, 1932; Loch, 1942). As noted by Homma et al. (2010), these characteristics are typical for structural stiffening, which is featured by a decrease at low frequencies and a shift of the resonance frequency to higher frequencies. The transition frequency between the low- and high-frequency behavior was a bit lower in our model than in most experiments, which is because the resonance frequency of our model without preload was slightly lower than average (0.77 kHz compared to ~1 kHz; see Fig. 9). The umbo and footplate results generally reflect the measurement data quite well (differences of generally less than 3 dB). For the footplate, however, the velocity change differed from the experimental average by up to 5 dB at –0.5 and –1 kPa (Fig. 10, bottom, right panel). At –0.5 kPa, the footplate response showed an increase relative to the unloaded condition, which was also observed by Murakami et al. (1997) in some temporal bones. Rasmussen (1946) and Bezold (1887) observed similar behavior for some human hearing thresholds, showing an optimal sensitivity under an ear-canal pressure of –0.6 kPa. Therefore, a small negative ear-canal pressure may optimize the stapes vibration in some individuals.

Fig. 10 revealed a small asymmetry in the umbo and footplate velocity change between positive and negative static pressure, with the highest decrease seen at positive pressure (difference of ~2.5 dB on average). This behavior has also been observed for normal hearing thresholds under static pressure (Hansen, 1955). When

comparing the left and right panels of Fig. 11, it can be deduced that the deformation of the geometry is mainly responsible for this asymmetry, as was found by Wang et al. (2007). Homma et al. (2010) showed that the overall stiffening of the TM components must be higher at positive than negative ear-canal pressure to replicate experimental data. By combining these findings, we conclude that the asymmetric stiffening associated with the deformed geometry is mainly a result of the TM shape. Homma et al. (2010) also found that the ligaments around the malleus (TTT, AML, LML and SML) must exhibit a higher stiffening at negative than positive ear-canal pressure. Based on these findings and the results of Wang et al. (2007) for the asymmetric stress level in the same components, Homma et al. (2010) suggested that the TM is strained most at positive pressure, while the ligaments around the malleus are strained most at negative pressure. These conclusions agree with our findings, where the average von Mises strain (a measure for the magnitude of the Green–Lagrange strain) in the TM was higher at a positive pressure of +4 kPa (1.7%) than at a negative pressure of –4 kPa (1.3%). The asymmetry of the strain was opposite for the ligaments around the malleus, with an average von Mises strain of 9.7% at +4 kPa and 15.5% at –4 kPa for the TTT, and 6.5% at +4 kPa and 13.4% at –4 kPa for the SML. The strain asymmetry of the AML and LML was less pronounced.

In Fig. 11, the relative influence of the underlying mechanisms of structural stiffening were evaluated. First, we deduced that the importance of each mechanism depends on the polarity of static pressure, the magnitude of static pressure, and the location in the ME. Second, we found that pressure-induced prestress has a substantial effect on structural stiffening and is not negligible as suggested by Wang et al. (2007). Third, we saw that including material nonlinearity does not always lead to a higher stiffening, which is in disagreement with earlier studies (Wang et al., 2007; Ihrle et al., 2013); at the umbo it led to a higher stiffening, but at the footplate it produced less stiffening. We note, however, that preceding studies used a different approach to quantify the effect of material nonlinearity. The lower stiffening at the footplate when including material nonlinearity was mainly due to the hyperelasticity of the SAL, which has a low Veronda–Westmann parameter $b = 0.214$. Compared to the linear elastic Saint-Venant Kirchhoff model that assumes a linear relationship between the second Piola-Kirchhoff stress $\mathbf{S}$ and Green–Lagrange strain $\mathbf{E}$, the stress $\mathbf{S}$ of the hyperelastic SAL model shows a slower increase with the strain $\mathbf{E}$ in the strain range covered by the simulations, hence leading to a less pronounced stiffening. At the umbo, the deformation behavior is governed more by the TM, of which the high Veronda–Westmann parameter $b = 22.02$ causes a higher increase of the stress (and hence stiffening) compared to the linear elastic case.

4.4 Elastic and viscoelastic properties of the middle-ear and joint components

In Fig. 12, we examined the effect of varying the hyperelastic and linear elastic parameters on the footplate magnitude without preload and the footplate velocity change under +1 and −1 kPa. The parameters of the TM and SAL had the highest effect on the structural stiffening behavior at low frequencies (Fig. 12, middle and bottom rows, left panel). Zhang et al. (2020) investigated the effect of varying the hyperelastic Ogden parameters (μ_1 and α_1) of the TM and SAL on the change in footplate vibration relative to the unloaded case under a preload of −2 kPa in the ME cavity (corresponding to a preload +2 kPa in the ear canal). Similar to our results of increasing μ_{TM} and μ_{SAL} by a factor 2 (Fig. 12, middle row, left panel), increasing μ_1 of the TM and SAL by a factor 5 in their study raised the footplate change curve at low frequencies. In Zhang et al (2020), changing μ_1 of the TM by a factor 1/5 led to a significant increase at all frequencies, except for a small decrease in the range 0.3–0.5 kHz. In our simulations, however, varying μ_{TM} by a factor 1/2 led to a decrease of the footplate change curve at 0.125 and 1 kHz (Fig. 12, middle row, left and middle panels). In Zhang et al. (2020), increasing α_1 of the SAL by a factor 5 had the highest effect, causing a significant reduction of the footplate change curve at low frequencies. Similarly, our results showed a decrease when b_{SAL} was increased by a factor 2 (Fig. 12, middle row, left panel). In Zhang et al. (2020), increasing α_1 of the TM by a factor 5 caused an increase at low frequencies, which is opposite to our findings when b_{TM} was increased by a factor 2 (Fig. 12, middle row, left panel). From Fig. 12 (middle and bottom rows), we can evaluate the relative influence of the b-parameters on the preloaded response under +1 and −1 kPa, which characterize the material nonlinearity of the ME components. We conclude that the material nonlinearity of the SAL is the most important, especially at low and mid frequencies. This finding can be understood by the observation that the SAL mainly governs the footplate behavior, and that the SAL experiences the highest static strain of all ME components. The material nonlinearities of the TM and joint capsules have a small but noticeable effect at +1 and −1 kPa. However, their influence may become more relevant at higher static pressures, as was the case for the static behavior (see Section 4.1). The material nonlinearities of the ligaments and tendons have minimal effect and thus seem unimportant.

In Figs. 13–15, we investigated the influence of the viscoelastic properties of the joint components on the ME vibration response. It was shown that the components of the IMJ have a considerably high effect (left panels), while the ISJ components have no meaningful impact with variations of less than 1 dB (right panels). For the IMJ capsule, increasing the shear modulus and relaxation coefficients (i.e., all g_i values of the joint in Table 2) reduced the umbo response but raised the footplate response at all frequencies in the unloaded condition (Fig. 13,

left, top panel). Experiments have shown that immobilizing the IMJ increases the footplate piston-like response at high frequencies (Gerig et al., 2015), which may reflect a similar behavior as increasing the stiffness of the IMJ when raising μ or g_i. As opposed to our model, however, their measurements showed on average no increase of the footplate response at low frequencies. For the IMJ synovial gap, the viscosity had a high effect on the ratio between the umbo and footplate magnitudes (Fig. 14, left, top panel), which amounted to 14 dB on average or a linear ratio of 5 in the base model. For the long-term static behavior, which is governed by elasticity and not by viscosity, the ratio between umbo and footplate displacement was about 19 dB or a linear ratio of 9 in the limit of zero static pressure (see Fig. 8). Although the static ratio decreases with static pressure to 14 dB at +4 and –4 kPa, the harmonic ratio decreases as well with static pressure in the presence of static preload (not shown), so the harmonic ratio remains lower than the static ratio at most frequencies. Hence, the static coupling of the malleus to the incus and stapes is weaker than the acoustic coupling. These findings suggest that the elastic compliance of the IMJ is partly responsible for decoupling the large static displacements of the malleus from the incus and stapes. On the other hand, the results suggest that the high viscosity and viscoelasticity of the IMJ could play a role in the transfer of sound-induced vibrations through the ME. This interpretation is similar to the conclusion of Ihrle et al. (2016, 2017), who investigated the viscoelastic behavior of the IMJ at low quasi-static operating speeds. They attributed the transfer of sound-induced ME vibrations to the high viscoelasticity of the ligaments in the IMJ capsule, which they modeled by distributing spring-damper elements arranged in parallel (Kelvin–Voigt elements) around the circumference of the IMJ body. In our simulations, viscoelasticity of the IMJ capsule alone was not sufficient to describe the ME sound transfer behavior, on which the viscosity of the synovial gap had a stronger influence. A constant viscosity of 10 Pa s was found to be appropriate to simulate the sound-transfer behavior, which was based on zero-shear viscosity data of healthy synovial fluid. In previous studies, lower viscosities of 0.01 Pa s (Gan and Wang, 2015) and 0.4 Pa s (Jiang and Gan, 2018) have been used to simulate the vibration response of the ISJ in the auditory range, and it was concluded by Jiang and Gan (2018) that the viscosity of the ISJ synovial fluid affects the ISJ dynamic behavior mostly at high frequencies. It is noted, however, that we used very soft solid elements with a constant viscosity-like parameter to mimic the fluid behavior of the synovial gaps. A valuable addition in the future could be to model the synovial gaps using actual fluid elements, although this would require modeling the dynamic behavior of the ME in the time domain in COMSOL. To verify our findings, experimental data of the viscoelastic properties of synovial fluid are needed at acoustic frequencies, which are currently lacking (Soleimani et al., 2020).

It has been proposed that the static decoupling characteristic of the flexible IMJ serves as a protective mechanism to shield the inner ear from excessive ossicle displacements (Hüttenbrink, 1988) or minimize sound-transfer loss under static pressure by preventing stiffening of the ME ligaments (Ihrle et al., 2017). In our simulations, increasing the stiffness of the IMJ capsule by a factor 10 caused an increase of the static footplate displacements (not shown) and a decrease of the footplate change curves under preloads of +1 and −1 kPa (Fig. 13, left, middle and bottom panels). However, the footplate magnitude in the absence of static preload was increased by the same amount as the decrease observed for the footplate change curves when the capsule stiffness was increased (Fig. 13, left, top panel). As a result, the overall footplate magnitude under preloads of +1 and −1 kPa was similar in the model with normal and increased IMJ stiffness. The same observation was made for higher static preloads (not shown). Based on these results, we cannot conclude that the IMJ serves to minimize sound-transfer loss under static preload.

5. Conclusion

In this study, we investigated the harmonic vibration behavior of the ME under large static pressures using 3D FE modeling. Before studying the preloaded harmonic response, we simulated the static deformation behavior and the harmonic response without preload by incorporating hyperelastic and viscoelastic properties of the ME, which were mainly based on measurement data. We found that viscoelasticity should be considered to describe the difference between the static and dynamic stiffness of the ME components, as it is needed to replicate both static and harmonic ME behavior.

For the harmonic response under static preload, we investigated which effects contribute to the observed structural stiffening of the ME. The deformed geometry caused asymmetry of the stiffening between positive and negative pressure, which is mainly a result of the inward cone shape of the TM. The prestress due to static pressure had a substantial impact on the stiffening, which is in disagreement with previous assumptions. Including material nonlinearity led to increased stiffening at the umbo but caused less pronounced stiffening at the footplate. The changes in footplate response under static pressure were mostly affected by the elastic properties of the TM and SAL, and material nonlinearity was most present in the SAL.

Finally, we examined the influence of the viscoelastic properties of the ossicular joints on the unloaded and preloaded ME response. The IMJ had a substantial impact on the harmonic behavior, while the ISJ had no meaningful effect. We found that the high flexibility of the IMJ enhanced the decoupling of static displacements

between umbo and footplate. At the same time, the results suggest that viscosity and viscoelasticity the IMJ could play a role in the sound transfer through the ME.

Declarations of competing interest

None.

Acknowledgments

We thank Dr. Daniël De Greef for his previous work that made this research possible.

Funding

This work was supported by the Research Foundation–Flanders (FWO) [grant number 1211920N].

References

Aibara, R., Welsh, J.T., Puria, S., Goode, R.L., 2001. Human middle-ear sound transfer function and cochlear input impedance. Hear. Res. 152, 100–109. https://doi.org/10.1016/S0378-5955(00)00240-9.

ASTM F2504-05, 2014. Standard practice for describing system output of implantable middle ear hearing devices. ASTM International, West Conshohocken, PA. https://doi.org/10.1520/F2504-05R14.

Başar, Y., Weichert, D., 2000. Nonlinear continuum mechanics of solids. Springer-Verlag Berlin Heidelberg. https://doi.org/10.1007/978-3-662-04299-1.

Bergevin, C., Olson, E.S., 2014. External and middle ear sound pressure distribution and acoustic coupling to the tympanic membrane. J. Acoust. Soc. Am. 135, 1294–1312. https://doi.org/10.1121/1.4864475.

Bezold, F., 1887. Statistiche Ergebnisse über die diagnostische Verwendbarkeit des Rinneschen Versuches. Ztschr. f. Ohrenheilk. 17, 153–237.

Bingöl, A.Ö., Lohmann, D., Püschel, K., Kulicke, W.-M., 2010. Characterization and comparison of shear and extensional flow of sodium hyaluronate and human synovial fluid. Biorheol. 47, 205–224. https://doi.org/10.3233/BIR-2010-0572.

Buytaert, J.A.N., Goyens, J., De Greef, D., Aerts, P., Dirckx, J.J.J., 2014. Volume shrinkage of bone, brain and muscle tissue in sample preparation for micro-CT and light sheet fluorescence microscopy (LSFM). Microsc. Microanal. 20, 1208–1217. https://10.1017/S1431927614001329.

Cheng, T., Dai, C., Gan, R.Z., 2007. Visoelastic properties of human tympanic membrane. Ann. Biomed. Eng. 35, 305–314. https://doi.org/10.1007/s10439-006-9227-0.

Cheng, T., Gan, R.Z., 2007. Mechanical properties of stapedial tendon in human middle ear. Transactions of the ASME. J. Biomech. Eng. 129, 913–918. https://doi.org/10.1115/1.2800837.

Cheng, T., Gan, R.Z., 2008a. Experimental measurement and modeling analysis on mechanical properties of tensor tympani tendon. Med. Eng. Phys. 30, 358–366. https://doi.org/10.1016/j.medengphy.2007.04.005.

Cheng, T., Gan, R.Z., 2008b. Mechanical properties of anterior malleolar ligament from experimental measurement and material modeling analysis. Biomech. Model. Mechanobiol. 7, 387–394. https://doi.org/10.1007/s10237-007-0094-x.

De Greef, D., Aernouts, J., Aerts, J., Cheng, J.T., Horwitz, R., Rosowski, J.J., Dirckx, J.J.J., 2014. Viscoelastic properties of the human tympanic membrane studied with stroboscopic holography and finite element modeling. Hear. Res. 312, 69–80. https://doi.org/10.1016/j.heares.2014.03.002.

De Greef, D., Buytaert, J.A.N., Aerts, J.R.M., Van Hoorebeke, L., Dierick, M., Dirckx, J., 2015. Details of human middle ear morphology based on micro-CT imaging of phosphotungstic acid stained samples. J. Morphol. 276, 1025–1046. https://doi.org/10.1002/jmor.20392.

De Greef, D., Pires, F., Dirckx, J.J.J., 2017. Effects of model definitions and parameter values in finite element modeling of human middle ear mechanics. Hear. Res. 344, 195–206. https://doi.org/10.1016/j.heares.2016.11.011.

Dirckx, J.J.J., Decraemer, W.F., 1991. Human tympanic membrane deformation under static pressure. Hear. Res. 51, 93–105. https://doi.org/10.1016/0378-5955(91)90009-X.

Dirckx, J.J.J., Decraemer, W.F., 2001. Effect of middle ear components on eardrum quasi-static deformation. Hear. Res. 157, 124–137. https://doi.org/10.1016/S0378-5955(01)00290-8.

Dobrev, I., Schär, M., Chatzimichalis, M., Prochazka, L., Pfiffner, F., Röösli, C., Huber, A.M., Sim, J.H., 2018. Intracochlear pressure change by the 3D motion components of the stapes [abstract]. In: Abstract Book of the 8th International Symposium on Middle-Ear Mechanics in Research and Otology. Shanghai, China, pp. 115–116.

Fam, H., Bryant, J.T., Kontopoulou, M., 2007. Rheological properties of synovial fluids. Biorheol. 44, 59–74.

Finkelstein, Y., Zohar, Y., Talrni, Y.P., Rubel, Y., Shanny, I., 1992. Effects of acute negative middle ear pressure on hearing; new answers to old questions and a review of the literature. Acta Otolaryngol. 112, 88–95.

Gan, R.Z., Wood, M.W., Dormer, KJ., 2004. Human middle ear transfer function measured by douple laser interferometry system. Otol. Neurotol. 25, 423–435. https://doi.org/10.1097/00129492-200407000-00005.

Gan, R.Z., Feng, B., Sun, Q., 2004. Three-dimensional finite element modeling of the human ear for sound transmission. Ann. Biomed. Eng. 32, 847–859. https://doi.org/10.1023/B:ABME.0000030260.22737.53.

Gan, R.Z., Dai, C., Wood, M.W., 2006. Laser interferometry measurement of middle ear fluid and pressure effects on sound transmission. J. Acoust. Soc. Am. 120, 3799–3810 https://doi.org/10.1121/1.2372454.

Gan, R.Z., Yang, F., Zhang, X., Nakmali, D., 2011. Mechanical properties of stapedial annular ligament. Med. Eng. Phys. 33, 330–339. https://doi.org/10.1016/j.medengphy.2010.10.022.

Gan, R.Z., Wang, X., 2015. Modeling microstructure of incudostapedial joint and the effect on cochlear input. AIP Conf. Proc. 1703, 060011. https://doi.org/10.1063/1.4939366.

Gerig, R., Ihrle, S., Röösli, C., Dalbert, A., Dobrev, I., Pfiffner, F., Eiber, A., Huber, A.M., Sim, J.H., 2015. Contribution of the incudo-malleolar joint to middle-ear sound transmission. Hear. Res. 327, 218–226. https://doi.org/10.1016/j.heares.2015.07.011.

Gyo, K., Goode, R.L., 1987. Effects of middle-ear pressure changes on umbo vibration. Auris Nasus Larynx 14, 131–137. https://10.1016/S0385-8146(87)80013-5.

Hansen, R., 1955. The effect of static air pressure in the external auditory meatus on hearing acuity. Tech. Rept. Wright Air Development Center Air Research and Development Command USAF, Wright Patterson Air Force Base, Ohio.

Homma, K., Shimizu, Y., Kim, N., Du, Y., Puria, S., 2010. Effects of ear-canal pressurization on middle-ear bone- and air-conduction responses. Hear. Res. 263, 204–215. https://doi.org/10.1016/j.heares.2009.11.013.

Huizing, E.H., 1960. Bone conduction-the influence of the middle ear. Acta Otolaryngol. Suppl. 155:1–99.

Hüttenbrink, K.-B., 1988. The mechanics of the middle-ear at static air pressures: the role of the ossicular joints, the function of the middle-ear muscles and the behaviour of stapedial prostheses. Acta Otolaryngol. 451, 1–35. https://doi.org/10.3109/00016488809099007.

Ihrle, S., Lauxmann, M., Eiber, A., Eberhard, P., 2013. Nonlinear modelling of the middle ear as an elastic multibody system—Applying model order reduction to acousto-structural coupled systems. J. Comput. Appl. Math. 246, 18–26. https://doi.org/10.1016/j.cam.2012.07.010.

Ihrle, S., Gerig, R., Dobrev, I., Röösli, C., Sim, J.H., Huber, A.M., Eiber, A., 2016. Biomechanics of the incudo-malleolar-joint—experimental investigations for quasi-static loads. Hear. Res. 340, 69–78. https://doi.org/10.1016/j.heares.2015.10.015.

Ihrle, S., Eiber, A., Eberhard, P., 2017. Modeling of the incudo-malleolar joint within a biomechanical model of the human ear. Multibody Syst. Dyn. 39, 291–310. https://doi.org/10.1007/s11044-016-9550-7.

Jiang, S., Gan, R.Z., 2018. Dynamic properties of the human incudostapedial joint—Experimental measurement and finite element modeling. Med. Eng. Phys. 54, 14–21. https://doi.org/10.1016/j.medengphy.2018.02.006.

Karmody, C.S., Northop, C.C., Levine, S.R., 2009. The incudostapedial articulation: new concepts. Otol. Neurotol. 30, 990–997. https://doi.org/10.1097/MAO.0b013e3181b0fff7.

Kim. B.-K., Youn, S.-K., 2001. A viscoelastic constitutive model of rubber under small oscillatory load superimposed on large static deformation. Arch. Appl. Mech. 71, 748–763. https://doi.org/10.1007/s004190100186.

Kurokawa, H., Goode, R.L., 1995. Sound pressure gain produced by the human middle ear. Otolaryngol. Head Neck Surg. 113, 349–355. https://doi.org/10.1016/S0194-5998(95)70067-6.

Lai, W.M., Kuei, S.C., Mow, V.C., 1978. Rheological equations for synovial fluids. J. Biomech. Eng. 100, 169–186. https://doi.org/10.1115/1.3426208.

Lee, C.-Y., Rosowski, J.J., 2001. Effects of middle-ear static pressure on pars tensa and pars flaccida of gerbil ears. Hear. Res. 153, 146–163. https://10.1016/s0378-5955(00)00269-0.

Lim, D.J., 1968. Tympanic membrane part II.: pars flaccida. Acta Otolaryngol. 66, 515–532. https://doi.org/10.3109/00016486809126316.

Lion, A., Retka, J., Rendek, M., 2009. On the calculation of predeformation-dependent dynamic modulus tensors in finite nonlinear viscoelasticity. Mech. Res. Commun. 36, 653–658. https://doi.org/10.1016/j.mechrescom.2009.02.005.

Loch, W.E., 1942. Effects of experimentally altered air pressure in the middle ear on hearing acuity. Ann. Otol. Rhinol. Laryngol. 51, 995–1006. https://doi.org/10.1177/000348944205100411.

Luo, H., Dai, C., Gan, R.Z., Lu, H., 2009. Measurement of Young's modulus of human tympanic membrane at high strain rates. J Biomech Eng Trans 131, 064501. https://doi.org/10.1115/1.3118770.

Maftoon, N., Funnell, W.R.J., Daniel, S.J., Decraemer, W.F., 2015. Finite-element modelling of the response of the gerbil middle ear to sound. JARO 16, 547–567. https://doi.org/10.1007/s10162-015-0531-y.

Mao, H., 2018. Chapter 12 - Modeling the head for impact scenarios. In: Yang, K.-H. (Ed.), Basic finite element method as applied to injury biomechanics, pp. 469–502. Academic Press. https://doi.org/10.1016/B978-0-12-809831-8.00012-X.

Merchant, S.N., Ravicz, M.E., Rosowski, J.J., 1996. Acoustic input impedance of the stapes and cochlea in human temporal bones. Hear. Res. 97, 30–45. https://doi.org/10.1016/S0378-5955(96)80005-0.

Merodio, J., Ogden, R., 2020. Constitutive modelling of solid continua. Springer: Cham. https://doi.org/10.1007/978-3-030-31547-4_2.

Morman, K.N., Nagtegaal, J.C., 1983. Finite element analysis of sinusoidal small-amplitude vibrations in deformed viscoelastic solids. Part I: theoretical development. Int. J. Numer. Methods Eng. 19, 1079–1103. https://doi.org/10.1002/nme.1620190712.

Motallebzadeh, H., Charlebois, M., Funnell, W.R.J., 2013. A non-linear viscoelastic model for the tympanic membrane. J. Acoust. Soc. Am. 134:4427–4434. https://doi.org/10.1121/1.4828831.

Motallebzadeh, H., Maftoon, N., Pitaro, J., Funnell, W.R.J., Daniel, S.J., 2017. Finite-element modeling of the acoustic input admittance of the newborn ear canal and middle ear. JARO 18, 25–48. https://doi.org/10.1007/s10162-016-0587-3.

Murakami, S., Gyo, K., Goode, R.L., 1997. Effect of middle ear pressure change on middle ear mechanics. Acta Otolaryngol. 117, 390–395. https://doi.org/10.3109/00016489709113411.

Muyshondt, P.G.G., Aerts, P., Dirckx, J.J.J., 2019. The effect of single-ossicle ear flexibility and eardrum cone orientation on quasi-static behavior of the chicken middle ear. Hear. Res. 378, 13–22. https://doi.org/10.1016/j.heares.2018.10.011.

Nakajima, H.H., Dong, W., Olson, E.S., Merchant, S.N., Ravicz, M.E., Rosowski, J.J., 2009. Differential intracochlear sound pressure measurements in normal human temporal bones. JARO 10, 23–36. https://doi.org/10.1007/s10162-008-0150-y.

Nishihara, S., Aritomo, H., Goode, R.L., 1993. Effect of changes in mass on middle ear function. Otolaryngol. Head Neck Surg. 109, 899–910. https://doi.org/10.1177/019459989310900520.

O'Connor, K.N., Cai, H., Puria, S., 2017. The effects of varying tympanic-membrane material properties on human middle-ear sound transmission in a three-dimensional finite-element model. J. Acoust. Soc. Am. 142, 2836–2853. https://doi.org/10.1121/1.5008741.

Puria, S., Peake, W.T., Rosowski, J.J., 1997. Sound-pressure measurements in the cochlear vestibule of human-cadaver ears. J. Acoust. Soc. Am. 101, 2754–2770. https://doi.org/10.1121/1.418563.

Rasmussen, H., 1946. Studies on the effect upon the hearing through air conduction brought about by variations of the pressure in the auditory meatus. Acta Otolaryngol. 34, 415–424. https://doi.org/10.3109/00016484609119536.

Rahm, W.E., Strother, W., Crump, J.F., 1956. The effects of pressure in the external auditory meatus. Ann. Otol. Rhinol. Laryngol. 65, 657–64. https://doi.org/10.1177/000348945606500307.

Rohani, S.A., Ghomashchi, S., Agrawal, S.K., Ladak, H.M., 2017. Estimation of the Young's modulus of the human pars tensa using in-situ pressurization and inverse finite-element analysis. Hear. Res. 345, 69–78. https://doi.org/ 10.1016/j.heares.2017.01.002.

Rosowski, J.J., Lee, C.-Y., 2002. The effect of immobilizing the gerbil's pars flaccida on the middle-ear's response to static pressure. Hear. Res. 378, 183–195. https://10.1016/S0378-5955(02)00655- X.

Sackmann, B., Dalhoff, E., Lauxmann, M., 2019. Model-based hearing diagnostics based on wideband tympanometry measurements utilizing fuzzy arithmetic. Hear. Res. 378, 126–138. https://doi.org/10.1016/j.heares.2019.02.011.

Safari, M., Bjelle, A., Gudmundsson, M., Högfors, C., Granhed, H., 1990. Clinical assessment of rheumatic diseases using viscoelastic parameters for synovial fluid. Biorheol., 27, 659–674. https://doi.org/10.3233/BIR-1990-27504.

Schurz, J., 1996. Rheology of synovial fluids and substitute polymers. J. Macromol. Sci. A Pure Appl. Chem. 33, 1249–1262. https://doi.org/10.1080/10601329608010919.

Shanks, J., Shelton, C., 1991. Basic principles and clinical applications of tympanometry. Otolaryngol. Clin. North. Am. 24, 299–328.

Soleimani, M., Funnell, W.R.J., Decraemer, W.F., 2020. A non-linear viscoelastic model of the incudostapedial joint. JARO 21, 21–32. https://doi.org/10.1007/s10162-019-00736-0.

Soons, J.A.M., Aernouts, J., Dirckx, J.J.J., 2010. Elasticity modulus of rabbit middle ear ossicles determined by a novel micro-indentation technique. Hear. Res. 263, 33–37. https://doi.org/10.1016/j.heares.2009.10.001.

Suehiro, M., 1990. Effects of an increase or decrease in the middle ear pressure on tympanic membrane vibration. J. Otolaryngol. Jpn. 93, 398–406. https://10.3950/jibiinkoka.93.398.

Van der Jeught, S., Dirckx, J.J.J., Aerts, J.R.M., Bradu, A., Podoleanu, A.G., Buytaert, J.A.N., 2013. Full-field thickness distribution of human tympanic membrane obtained with optical coherence tomography. JARO 14, 483–493. https://doi.org/ 10.1007/s10162-013-0394-z.

Veronda, D.R., Westmann, R.A., 1970. Mechanical characterization of skin—Finite deformations. J. Biomech. 3, 111–122. https://doi.org/10.1016/0021-9290(70)90055-2.

Volandri, G., Di Puccio, F., Forte, P., Carmignani, C., 2011. Biomechanics of the tympanic membrane. J. Biomech. 44, 1219–1236. https://doi.org/10.1016/j.jbiomech.2010.12.023.

von Békésy, G., 1932. Zur Theorie des Hörens bei der Schallaufnahme durch Knochenleitung. Ann. Phys. 13, 111–136. https://doi.org/10.1002/andp.19324050109.

Wang, X., Cheng, T., Gan, R.Z., 2007. Finite-element analysis of middle-ear pressure effects on static and dynamic behavior of human ear. J. Acoust. Soc. Am. 122, 906–917. https://doi.org/10.1121/1.2749417.

Wever, E.G., Lawrence, M., 1954. Physiological acoustics. Princeton: Princeton University Press.

Zeidler, H., Altmann, S., John, B., Gaffga, R., Kulicke, W.-M., 1979. Rheologie pathologischer Gelenkflüssigkeiten. 1. Weitere Ergebnisse zur Visko-elastizität. Rheol. Acta 18, 151–167. https://doi.org/10.1007/BF01515699.

Zhang, X., Gan, R.Z., 2011. Experimental measurement and modeling analysis on mechanical properties of incudostapedial joint. Biomech. Model. Mechanobiol. 10, 713–726. https://doi.org/0.1007/s10237-010-0268-9.

Zhang, X., Gan, R.Z., 2013a. Dynamic properties of human tympanic membrane based on frequency-temperature superposition. Ann. Biomed. Eng. 41, 205–214. https://doi.org/10.1007/s10439-012-0624-2.

Zhang, X., Gan, R.Z., 2013b. Finite element modeling of energy absorbance in normal and disordered human ears. Hear. Res. 301, 146–155. https://doi.org/10.1016/j.heares.2012.12.005.

Zhang, X., Gan, R.Z., 2014. Dynamic properties of human stapedial annular ligament measured with frequency-temperature superposition. J. Biomech. Eng. 136, 0810041–0810047. https://doi.org/10.1115/1.4027668.

Zhang, J., Jiao, C., Zou, D., Ta, N., Rao, Z., 2020. Assigning viscoelastic and hyperelastic properties to the middle-ear soft tissues for sound transmission. Biomech. Model. Mechanobiol. 19, 957–970. https://doi.org/10.1007/s10237-019-01263-w.